

# 3D Reconstruction of Neuronal Allometry and Neuromuscular Projections in Asexual Planarians Using Expansion Tiling Light Sheet Microscopy

Jing Lu, Hao Xu, Dongyue Wang, Yanlu Chen, Takeshi Inuoe, Liang Gao , Kai Lei 

College of Life Sciences, Zhejiang University, Hangzhou, Zhejiang, China • Key Laboratory of Structural Biology of Zhejiang Province, School of Life Sciences, Westlake University, Hangzhou, Zhejiang, China • Westlake Laboratory of Life Sciences and Biomedicine, Hangzhou, Zhejiang, China • Key Laboratory of Growth Regulation and Translational Research of Zhejiang Province, School of Life Sciences, Westlake University, Hangzhou, Zhejiang, China • Institute of Biology, Westlake Institute for Advanced Study, Hangzhou, Zhejiang, China • Division of Adaptation Physiology, Faculty of Medicine, Tottori University, Yonago, Japan

 [https://en.wikipedia.org/wiki/Open\\_access](https://en.wikipedia.org/wiki/Open_access)

 Copyright information

## eLife Assessment

This **useful** study presents a novel microscopy technique called "Expansion Tiling Light Sheet Microscopy" and an accompanying computational pipeline for the faster collection and analysis of 3D volumetric images in animals like planarians. This approach produces beautiful 3D microscopy images and is **solid** on a technical level. However, due to the use of antibody reagents that visualize many – but not all – neurons and muscle subtypes, the evidence for the biological conclusions in this study remains **incomplete**. With the claims appropriately contextualized, this paper will be of interest to cell biologists working on imaging and analyzing whole animals.

<https://doi.org/10.7554/eLife.101103.1.sa4>

## Abstract

### Abstract

The intricate coordination of the neural network in planarian growth and regeneration has remained largely unrevealed, partly due to the challenges of imaging the central nervous system (CNS) in three dimensions (3D) with high resolution and within a reasonable timeframe. To address this gap in systematic imaging of the CNS in planarians, we adopted high-resolution, nanoscale imaging by combining tissue expansion and tiling light-sheet microscopy, achieving up to 4-fold linear expansion. Using a semi-automatic 3D cell segmentation pipeline, we quantitatively profiled neurons and muscle fibers at the single-cell level in over 400 wild-type planarians during homeostasis and regeneration. We validated previous observations of neuronal cell number changes and muscle fiber distribution. We

found that the rate of neuron cell proliferation tends to lag behind the rapid expansion of somatic cells during the later phase of homeostasis. By imaging the planarian with up to 120 nm resolution, we also observed distinct muscle distribution patterns at the anterior and posterior poles. Furthermore, we investigated the effects of  $\beta$ -catenin RNAi on muscle fiber distribution at the posterior pole, consistent with changes in anterior-posterior polarity. The glial cells were observed to be close in contact with dorsal-ventral muscle fibers. Finally, we observed disruptions in neural-muscular networks in *inr-1* RNAi planarians. These findings provide insights into the detailed structure and potential functions of the neural-muscular system in planarians and highlight the accessibility of our imaging tool in unraveling the biological functions underlying their diverse phenotypes and behaviors.

## Introduction

The central nervous system (CNS) stands as a marvel of intricate organization, enabling the execution of complex functions crucial for an organism's survival (Cajal, 1995 [↗](#)). It is the hub for processing and coordinating information throughout the body, employing specialized regions with distinct structures and functions (Bullock and Horridge, 1965 [↗](#)). However, the regenerative capacity of the CNS poses a formidable challenge, as it exhibits limited ability for de novo regeneration (Obernier et al., 2014 [↗](#)).

The planarian CNS is a fascinating model for studying neural regeneration (Agata et al., 1998 [↗](#)). Planarians are flatworms that possess a relatively simple CNS, yet they have an impressive ability to regenerate their neural tissue. The planarian CNS is organized into different molecular and functional domains defined by the expression of specific neural genes (Cebrià et al., 2022 [↗](#)). Planarians can regenerate functional brains from even tiny body fragments, highlighting their remarkable regenerative capabilities (Umesono et al., 2009 [↗](#)). This unique regenerative potential is attributed to the presence of pluripotent stem cells called neoblasts, which can differentiate into various cell types, including neurons (Cebrià et al., 2007 [↗](#)). The availability of hundreds of genes expressed in planarian neurons, coupled with the ability to silence them through RNA interference, has facilitated the unraveling of the molecular mechanisms underlying CNS regeneration in these organisms (Cebrià et al., 2007 [↗](#)). The study of planarian CNS regeneration provides valuable insights into the fundamental processes of neural regeneration, which may have implications for regenerative medicine and understanding human nervous system repair.

Understanding the mechanisms underlying CNS regeneration requires applying powerful tools to study its structure and organization at the cellular to sub-cellular levels. Advanced imaging techniques, including high-resolution microscopy, offer exceptional opportunities to gain invaluable insights into the intricate architecture of the CNS. Gained from both advanced imaging techniques, researchers can harness knowledge from the regenerative wonders observed in nature that hold promise for promoting CNS regeneration (Dott et al., 2007; Tomer et al., 2011 [↗](#)). However, the intricate network and the dynamics of planarian CNS have remained largely unrevealed due to the challenges of imaging the CNS in 3D with high resolution within a reasonable timeframe.

Tiling light sheet microscopy is a flexible imaging technique that has been adapted for use in live organisms and cleared tissues (Gao, 2015 [↗](#); Fu et al., 2016 [↗](#)). Its flexible multicolor 3D imaging ability has been shown across a variety of samples, from structures as complex as the mouse spinal cord to the intricate tissues of planarians (Chen et al., 2020 [↗](#); Xie et al., 2023 [↗](#)). In TLSM, a thin and focused light sheet is used to illuminate the sample from the side, exciting fluorophores close to the focal plane. By tiling the light sheet within the imaging field of view at multiple positions and using the images generated by the thinnest section of the light sheet, researchers can create a comprehensive and high-resolution image of the entire sample. This method combines the benefits of light sheet microscopy, which offers high spatial resolution and imaging speed, with

tiling capabilities to capture larger samples (Chen et al., 2020 [DOI](#)). This technique is particularly useful for imaging cleared tissues, enabling rapid multicolor 3D imaging with micron-scale to submicron-scale spatial resolution (Chen et al., 2020 [DOI](#)). Expansion microscopy has been employed in planarian studies for the detailed visualization of neuronal structures (Wang et al., 2016 [DOI](#); Khariton et al., 2020 [DOI](#)). It remained a challenge to image the entire CNS in 3D at high resolution within a reasonable time frame. While tissue clearing is a common practice in microscopy, we found it particularly useful as a pre-expansion treatment for lipid-rich samples such as planarians. This process allows homogenization without the need for heating or proteinase treatment. C-MAP was able to preserve the natural proteins during expansion, which allows the use of conventional FISH and antibody staining. The combination of C-MAP and tiling light sheet microscopy has achieved improved 3D resolution, signal-to-noise ratio, and sample compatibility (Chen et al., 2015 [DOI](#); Ku et al., 2016 [DOI](#); Tillberg et al., 2016 [DOI](#); Chang et al., 2017 [DOI](#); Gao et al., 2019 [DOI](#); Wassie et al., 2019 [DOI](#)). TLSM has greatly advanced our understanding of complex biological systems and has opened new possibilities for studying cellular dynamics and interactions within multicellular organisms (Gao, 2015 [DOI](#); Fu et al., 2016 [DOI](#)). The combination of TLSM and C-MAP suggests a potential method to study the regenerative CNS in planarian and other non-traditional model organisms.

In this study, we applied TLSM and C-MAP to record the planarian spatial information at single cellular or higher resolution levels. We present a 3D tissue reconstruction method to investigate neuron type diversity and development at the single-cell level by labeling various neuron types, including cholinergic, GABAergic, octopaminergic, dopaminergic, and serotonergic neurons. We successfully quantitatively profiled neurons at the single-cell level in over 400 wild-type planarians during homeostasis and regeneration. In addition to obtaining higher-resolution images of known structures within planarians, such as muscles, we also discovered previously unreported muscle-muscle and neuron-muscle connections. We further provided evidence that suggests muscle fibers as a scaffold for targeted neuron projection. These results are of significant interest as they contribute to our understanding of how the primitive CNS coordinates the behavior and the underlying mechanism involved in the precise regeneration of neurons and their networks.

## Results

### Establishment of 3D tissue reconstruction using expansion tiling light sheet microscopy for planarian *Schmidtea mediterranea*

We first set up the experiment pipeline utilizing Clearing and Magnification Analysis of Proteome (C-MAP) for planarian expansion and tiling light-sheet microscope for imaging (Figure 1A [DOI](#)). The expansion procedure was performed after the conventional staining in planarians (Chen et al., 2020 [DOI](#)). To improve the efficiency of sample processing, we have made several modifications to the original protocol (Figure 1A [DOI](#)). Firstly, we incorporated tissue clearing to ensure uniform homogenization of the entire planarian. Secondly, instead of relying on the conventional gelation incubation at 37°C, we expedited gelation by exposing the samples to violet light for 30 seconds. Thirdly, we conducted the procedure on ice to minimize the impact of high-temperature gelation. Lastly, for smaller samples, we reduced or eliminated the time required for tissue clearing. Two spatial resolutions were adopted to image expanded planarians,  $2 \times 2 \times 5 \mu\text{m}^3$  and  $0.5 \times 0.5 \times 1.6 \mu\text{m}^3$ . The resolution can be further improved to 500 nm and 120 nm with 4× expansion, respectively. The total hours required for expansion and imaging were summarized (Figure S1A). In the case of a 2 mm planarian, imaging at  $2 \times 2 \times 5 \mu\text{m}^3$  spatial resolution requires approximately 1 hour with dual channel imaging. Imaging at  $0.5 \times 0.5 \times 1.6 \mu\text{m}^3$  resolution requires about 12 hours. The individual images were able to be conveniently integrated into a 3D tiff. file (Figure S1B). After all, we believe it is a practical pipeline to image planarians in 3D with high resolution within an acceptable time frame.

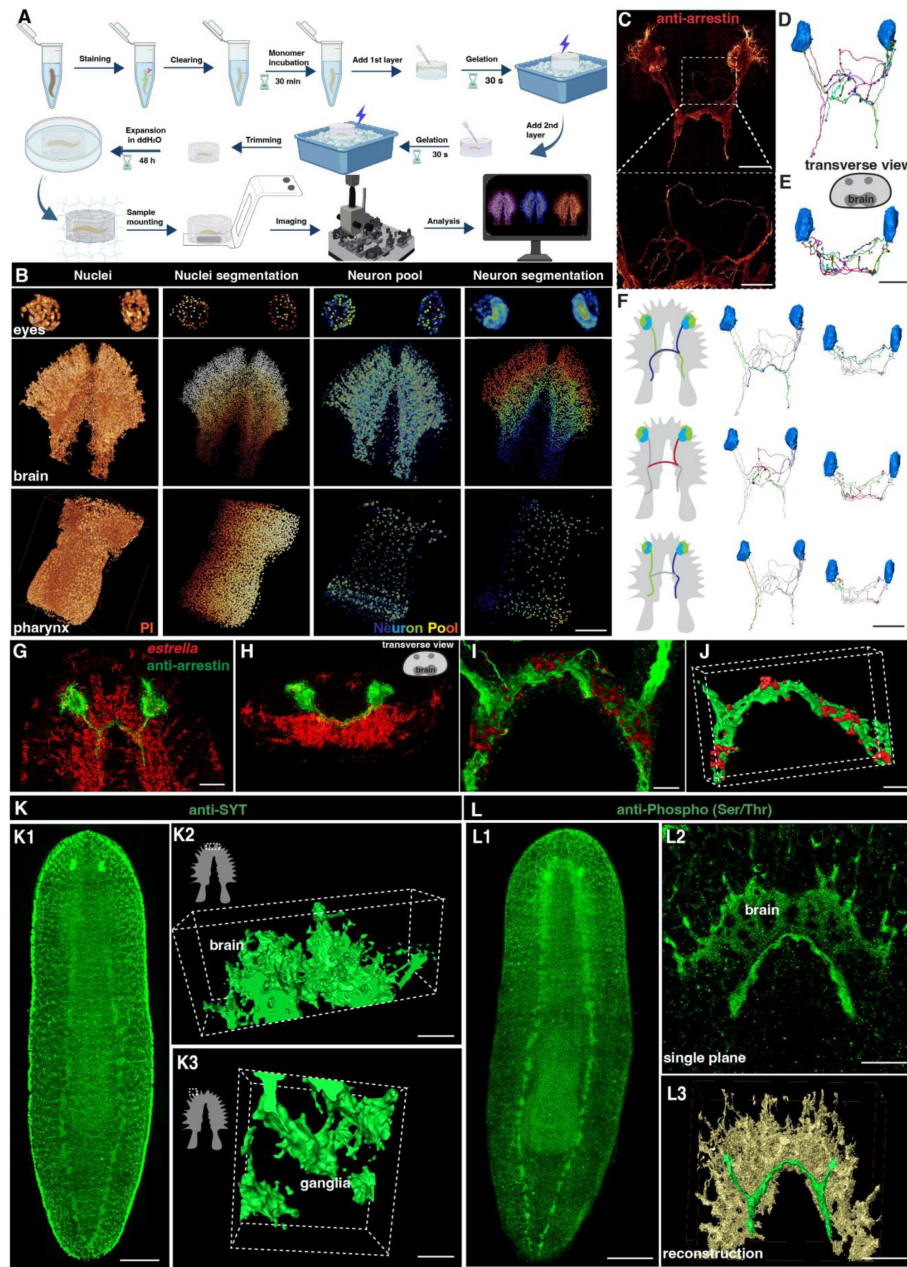


**Figure 1.**

Tiling light sheet microscopy for imaging planarian central nervous system (CNS). (A) Planarian expansion workflow. Planarians were fixed and stained with FISH or immunostaining, followed by tissue expansion and tiling light sheet microscopy imaging. Created with Biorender. (B) Segmentation of PI and neuron pool riboprobes labeled cells in eyes, brain, and pharynx. Scale bar, 600  $\mu$ m. (C) Staining of anti-arrestin antibody for the planarian visual system. Scale bar, 600  $\mu$ m. The lower image shows a magnification of the selected area in the upper image. Scale bar, 200  $\mu$ m. (D) Neuron tracing of the upper image in panel C. (E) Tracing of single neurons in transverse view. Scale bar, 600  $\mu$ m. (F) Traced axon projection trajectories from each eye. Scale bar, 600  $\mu$ m. (G) Dual staining of glial cells (*estrella*<sup>+</sup>) and visual system (anti-arrestin<sup>+</sup>) in the head region of a wild-type planarian. Scale bar, 350  $\mu$ m. (H) Xz view of the image in panel G. (I) Zoom in of panel G shows the glial cells close to the visual axons. Scale bar, 100  $\mu$ m. (J) Reconstruction of the glial and visual system. Scale bar, 100  $\mu$ m. (K1) Anti-SYT staining in a wild-type planarian. Scale bar, 600  $\mu$ m. (K2) The 3D reconstructed image of ganglia in the anterior tip of the brain. Scale bar, 120  $\mu$ m. (K3) The 3D reconstructed image of ganglia in the branch region of the brain. Scale bar, 30  $\mu$ m. (L1) Anti-Phospho (Ser/Thr) staining in a wild-type planarian. Scale bar, 600  $\mu$ m. (L2) Single plane image of the brain. Scale bar, 150  $\mu$ m. (L3) 3D reconstruction of brain region. Green represents the visual neurons, and yellow represents the brain. Scale bar, 180  $\mu$ m.



We next set up the pipeline of 3D tissue reconstruction and cell segmentation for planarian CNS. To accurately count individual cells, we developed a semi-automatic cell-counting pipeline to segment various planarian tissues and individual cells, including a plane section of the head, a layer of epidermis, and the whole organ of the pharynx (Figure S1C-P). This pipeline detects cell boundaries and assigns labels to each cell, thus facilitating accurate cell counting (Figure S1C-G, Q-T, Supplemental video 1). By employing Fluorescence in Situ Hybridization (FISH), we successfully visualized a variety of planarian neurons, including cholinergic (*chat*<sup>+</sup>), serotonergic (*tph*<sup>+</sup>), octopaminergic (*tbh*<sup>+</sup>), GABAergic (*gad*<sup>+</sup>), and dopaminergic (*th*<sup>+</sup>) neurons (Figure S2A, Supplemental video 2) (Currie et al., 2016 [DOI](#)). Segmentation of each neuron type showed their spatial atlas in the head (Figure S2B). The combination of these five types of neurons constitutes a neuron pool that enables the labeling of all neurons throughout the entire body, including the eyes, brain, and pharynx (Figure 1B [DOI](#)). Similarly, the *estrella*<sup>+</sup> glial cells can be visualized and segmented (Figure S2C). The segmentation pipeline applied at 160 nm resolution at the single cell level was achieved for the nucleus and the cell body of neurons.

To visualize the neural network, we further stained the anti-arrestin to image the visual projections (Figure 1C-E [DOI](#), Supplemental video 3). We traced the trajectories of the photoreceptor axons, corroborating the existence of both ipsilateral and contralateral projections (Figure 1F [DOI](#)). Photoreceptor axons displayed the trajectories either to the contralateral or the ipsilateral side of the brain. Choice points were observed at the optic chiasm, consistent with the previous description (Agata et al., 1998 [DOI](#); Scimone et al., 2020 [DOI](#)). Glial cells have been observed to be closely associated with neurons in the brain region (Wang et al., 2016 [DOI](#); Roberts-Galbraith et al., 2016 [DOI](#)). Additionally, it has been reported that glial cells might assist in the projection of photoreceptors (Chandra et al., 2023 [DOI](#)). To validate these observations, we performed co-staining of anti-arrestin and *estrella* (Figure 1G, H [DOI](#)). Our results consistently showed a strong association between glial cells and the projections of photoreceptors in the brain region (Figure 1I, J [DOI](#)). To visualize the neuronal network of the planarian, we used antibody staining with anti-SYT (Figure 1K [DOI](#)) and anti-Phospho (Ser/Thr) (Figure 1L [DOI](#)), respectively. Both anti-SYT and anti-Phospho (Ser/Thr) staining effectively stained the planarian brain and ventral nerve cord (VNC), therefore facilitating the observation of the planarian neuron network. Above all, we developed a platform for digital documentation and exploration of planarian CNS structures.

## Cell counting reveals a potential threshold in the increase of neuron numbers during planarian growth

Our method allows for a comprehensive quantitative analysis of the cell number change. Planarians ranging in length from 1 mm to 10 mm were carefully selected during the homeostatic phase to model planarian growth (Figure 2A [DOI](#), Figure S3A). In total, 99 samples were analyzed for 3D tissue reconstruction and cell segmentation. Images of alive planarians were captured, and accurate length was measured. By dual staining of the neuron pool and propidium iodide (PI), 3D images of the planarians were analyzed to measure the volume, length, width, and depth of all planarians, and numbers of whole-body cells and neurons (Figure 2B, C [DOI](#)). The volume and surface areas were quantified, revealing a consistent ratio of the square root of surface area to the cube root of volume during homeostasis (Figure S3B). The cell number-to-volume ratio remained stable in planarians during homeostasis (Figure S3C). Furthermore, brain volumes were measured, and brain volume increases proportionally with the growth of body length and volume (Figure S3D, E). Our results indicate the ability of planarians to flexibly regulate their cell number and scale of surface area relative to volume to adapt to the developmental changes during homeostasis.

Previous studies reported that body cells increase in number in correlation with planarian size growth through quantitative western blotting of worm lysates and image-based cell counting of dissociated worm (Thommen et al., 2019 [DOI](#)). In this study, we sought to validate this quantification at the single-cell level in intact planarians. We calculated the neuron numbers and cell numbers in

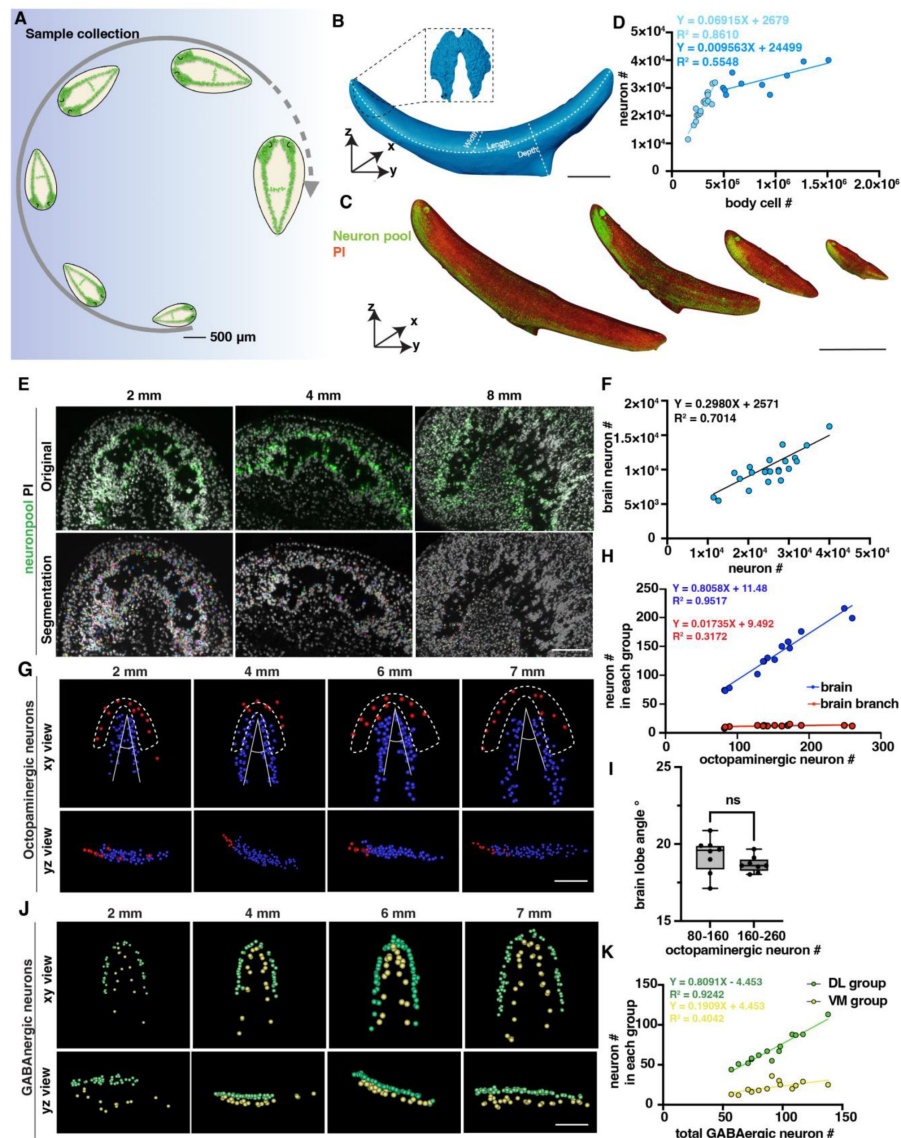


**Figure 2.**

Changes in the number of planarian neurons during homeostasis. **(A)** Workflow of sample collection of homeostatic planarians. Scale bar, 500  $\mu$ m. **(B)** 3D reconstruction of a planarian with PI staining. Length, volume, and surface area were measured using reconstructed images. The planarian brain is segmented and shown in a black dotted box. Scale bar, 2700  $\mu$ m. **(C)** Representative fluorescent images of planarians stained with neuron pool riboprobes and PI at sizes of 2 mm, 4 mm, 6 mm, and 8 mm. Scale bar, 6000  $\mu$ m. **(D)** Dot plot shows the correlation of whole-body cell number with neuron number in different sizes of intact planarians during homeostasis. Two trendlines are shown to represent planarians with differing cell counts. **(E)** Zoomed grayscale (PI) and segmented neurons (green) of selected brain regions of planarians at sizes of 2 mm, 4 mm, and 8 mm. Scale bar, 450  $\mu$ m. **(F)** Correlation of total neuron number with neuron number in brains in different sizes of intact planarians. **(G)** Segmented images of octopaminergic neurons in the main brain region (blue) and brain branch region (red) of planarians with the indicated body length are shown with xy and yz views. Scale bar, 900  $\mu$ m. **(H)** Dot plot shows the correlation of the total number of octopaminergic neurons with the octopaminergic neuron number in the brains (blue dots) and branches (red dots). **(I)** The plot illustrates the correlation between the angle of the brain lobe and the number of octopaminergic neurons in two groups of intact planarians: one with 80-160 octopaminergic neurons and the other with 160-220 octopaminergic neurons.  $n=8$  in each condition. The data is shown as the mean  $\pm$  SEM. Statistical significance was evaluated using the two-tailed unpaired Student's t-test, with  $**p < 0.01$ ,  $***p < 0.001$  indicating significance, while ns indicates lack of significance. **(J)** Segmented images of GABAergic neurons in the brains of planarians with the indicated body length are shown with xy and yz views. Scale bar, 900  $\mu$ m. **(K)** Dot plot shows the correlation of the total number of GABAergic neurons with the GABAergic neuron number in the VM region (yellow dots) and DL region (green dots).

planarians with different sizes, including neurons specifically located in the brain (**Figure 2D-F**). We observed a proportional increase in the total count of neuron cells with the overall size of the body, comprising approximately 10% of the total body cells when the length is shorter than 7 mm (**Figure 2D**). Dividing the planarians into 2-6 mm and 7-9 mm groups, we observed that the neuron number to cell number ratio is significantly higher in the 2-6 mm planarian group (**Figure S3F**). However, it is important to mention that the number of neurons in the brain exhibits a linear increase with overall neuron count (**Figure 2F**). Beyond this threshold, the proportion of neurons in the brain relative to the total cell population decreases (**Figure 2D**). Referring to the images, the decreased ratio in large planarians may be caused by the reduced density of neurons in the brain (**Figure 2E**). These findings provide evidence to support the previous prediction and consistency between different planarian species, and also suggest the existence of a threshold in the increase of planarian neuron numbers, which may ultimately contribute to some physiological changes such as planarian fission. We further analyzed different neuron types to examine their correlation with the increase in body size. Within the five types of neurons, we noticed that GABAergic, serotonergic, dopaminergic, and octopaminergic neurons increase in linear to the total cell number (**Figure S3G-J**). Since the pattern of cholinergic neurons is the major cell population in the brain, these results suggest that the above observation of the non-linear dynamics between neurons and cell numbers is likely from the cholinergic neurons. We further analyzed the octopaminergic neurons in the brain and branch regions (**Figure 2G**) and the GABAergic neurons in the ventral medial (VM) and the dorsal lateral (DL) regions (**Figure 2J**) (Nishimura et al., 2008; Currie et al., 2016). By quantifying these two groups, we found that the number of octopaminergic neurons in the brain increased concurrently with the overall increase of octopaminergic neurons; in contrast, the number of octopaminergic neurons in the branch region did not show a noticeable increase (**Figure 2H**). Additionally, the range of the angle of the brain lobe is around 17.12°-20.88° (**Figure 2I**). Similarly, the proportion of dorsal lateral GABAergic neurons increased relative to the total number of GABAergic neurons; in contrast, the increase rate of the VM region neurons was much higher than the rate of the DL region (**Figure 2K**). These findings indicate that octopaminergic and GABAergic neurons in different locations may be controlled by distinct mechanisms for their growth.

## Differential increase trends by neuron types during planarian regeneration

To comprehensively observe the dynamic changes of the neuron population during regeneration in *S. med*, an experiment was conducted using the tail fragments of 5-6 mm-long planarians by cutting their posterior tails into 2 mm fragments. Over a period of 14 days, daily fixation of planarian fragments was carried out. Four planarian fragments were analyzed at each time point (**Figure 3A**, **Figure S4A**). Similar to homeostasis, a consistent surface area-to-volume ratio was maintained in the regenerative processes (**Figure 3B**, **Figure S4B**). We further segmented the brain during regeneration and found that the brain size increased during the 14-day regeneration period (**Figure S4C**). To subsequently analyze each neuron type, probes such as *chat*, *gad*, *tbh*, *tph*, *th*, and PI were used to stain the regenerating fragments (**Figure S4E**). In total, 251 samples were analyzed for 3D tissue reconstruction and cell segmentation.

Previous studies have shown that the balance of cell numbers in planarians is influenced by cell proliferation, differentiation, and cell death during regeneration (Eisenhoffer et al., 2008; Takeda et al., 2009; Arnold et al., 2019; Oviedo et al., 2003; Hill et al., 2015). Cell numbers were counted from 0 to 14 days post-amputation (dpa). Cholinergic and serotonergic neurons were present not only in the brain but also distributed across the body's superficial layers (**Figure 3C**, **Figure S4D**). The count of cholinergic neurons initially started at ~ 7000 and continued to increase throughout the entire 14-day regeneration period (**Figure 3D**). For serotonergic neurons, they showed a similar pattern to cholinergic neurons (**Figure 3E**). GABAergic, octopaminergic, and dopaminergic neurons began to appear around days 3 and 4. Subsequently, the number of these neurons increased and reached a plateau after day 10 (**Figure 3F**, **Figure S4D**). It was reported

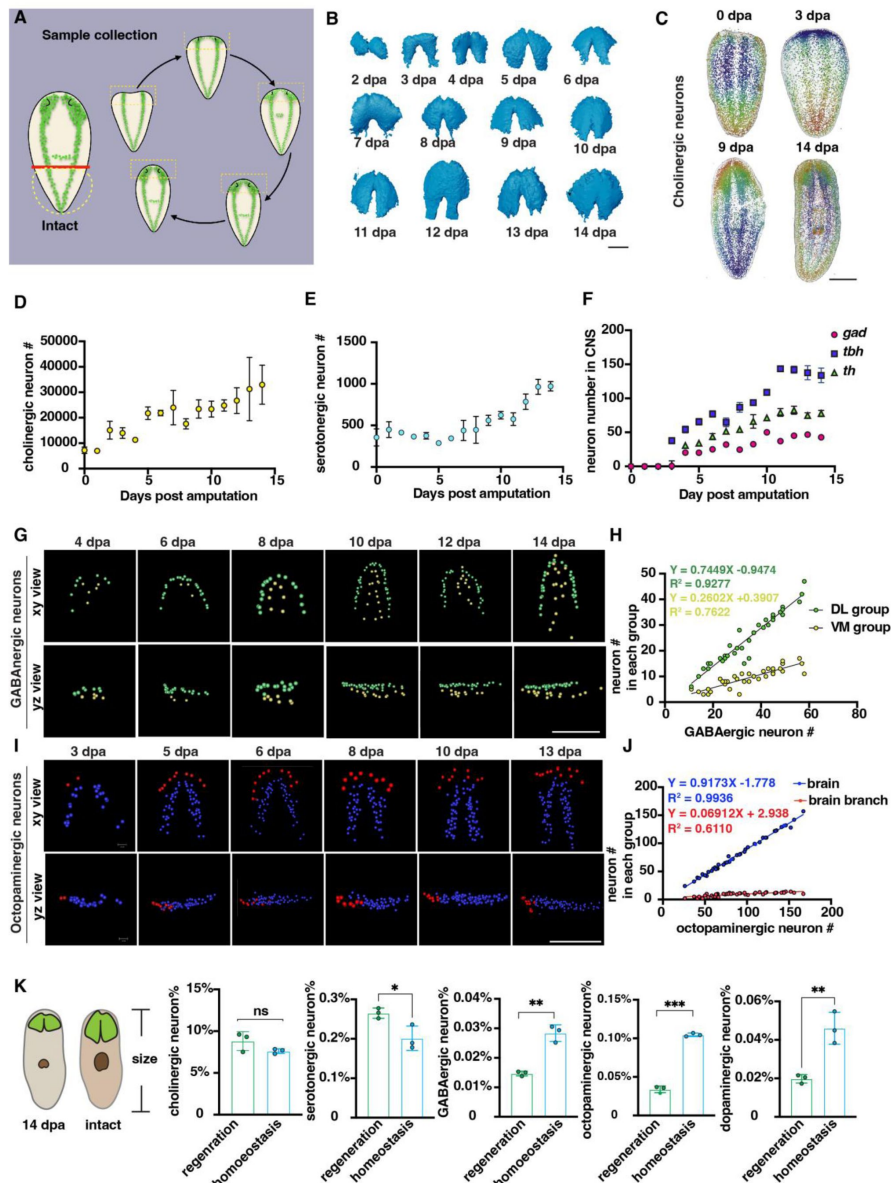


**Figure 3.**

Changes in the number of planarian neurons during regeneration. **(A)** Workflow of sample collection of regenerative planarians. **(B)** Reconstructed 3D brains segmented from PI-labeled regenerative tail fragments at various time points post-amputation. Scale bar, 900  $\mu$ m. **(C)** Representative xy views of segmented cholinergic neurons on 0-, 3-, 9-, and 14-days post-amputation. Scale bar, 1500  $\mu$ m. **(D)** Dot plot shows the increase of cholinergic neurons (*chat*) at different time points after amputation.  $N \geq 3$  in each condition. The data is shown as the mean  $\pm$  SEM. **(E)** Dot plot shows the increase of serotonergic neurons (*tph*) at different time points after amputation.  $N \geq 3$  in each condition. The data is shown as the mean  $\pm$  SEM. **(F)** Dot plot shows the increase of GABAergic (*gad*), octopaminergic (*tbh*), and dopaminergic (*th*) neurons at different time points after amputation.  $N \geq 3$  in each condition. The data is shown as the mean  $\pm$  SEM. **(G)** Representative xy and yz views of segmented GABAergic neurons on 4, 6, 8, 10, 12, and 14-day post-amputation. Scale bar, 900  $\mu$ m. **(H)** Dot plot shows the correlation of the total number of brain GABAergic neurons with the neuron number in the VM region (yellow dots) and DL region (green dots) in regenerative planarians. **(I)** Representative xy and yz views of segmented octopaminergic neurons on 3, 5, 6, 8, 10, and 13 days post-amputation. Scale bar, 900  $\mu$ m. **(J)** Correlation of the total number of the brain octopaminergic neurons with the octopaminergic neuron number in the brains (blue dots) and branches (red dots) in regenerative planarians. **(K)** Percentage of each type of neuron in the total cell number between 14 dpa planarians and the same size homeostatic planarians. Statistical significance was assessed by the two-tailed unpaired Student's t-test:  $^{**}p < 0.01$ ,  $^{***}p < 0.001$ ; ns, not significant.



that neurons exhibit an increase phase and plateau phase during planarian regeneration in *Dugesia japonica* (Takeda et al., 2009 [DOI](#)). Our results showed the similar pattern of neuron regrowth with two distinct phases, including an initial increasing phase (0-10 dpa) followed by a plateau phase (10-14 dpa).

Due to the linear and non-linear dynamics between neuron number and cell number in homeostatic growth, we further examined the dynamics of cell growth during regeneration. The GABAergic neurons in the VM and DL regions showed patterning on 4 dpa (Figure 3G [DOI](#)). The growth of DL and VM GABAergic neurons occurs proportionally during regeneration, in which the DL GABAergic neurons increase faster than the VM GABAergic neurons (Figure 3H [DOI](#)). In contrast, the octopaminergic neurons in the brain and branch regions began to appear on 3 dpa (Figure 3I [DOI](#)). Similarly, the number of octopaminergic neurons in the brain region increases proportionally, while those in the branch region continue to increase until reaching a number of 15 at 13 or 14 dpa (Figure 3J [DOI](#)). However, the number of octopaminergic neurons in the branch region only showed a slight fluctuation around 15-20 (Figure 3J [DOI](#)). Moreover, the angle of octopaminergic neurons in the brain decreased during regeneration and stabilized at 20°, which remained consistent during homeostasis (Figure S4E, Figure 2I [DOI](#)). These findings suggest that the reconstruction of DL, VM, branch, and main brain regions in planarians initiates concomitantly with the appearance of GABAergic and octopaminergic neurons. We further compared the ratio of different neuron types between planarians of the same body size at 14 dpa and in homeostasis. Our analysis revealed that the ratio of cholinergic and serotonergic neurons remained relatively constant in homeostasis. Conversely, the ratio of GABAergic, octopaminergic, and dopaminergic neurons is significantly lower in regeneration than in homeostatic planarians (Figure 3K [DOI](#)). Different populations of neurons exhibit diverse growth patterns during the process of regeneration (Takeda et al., 2009 [DOI](#)). Our results provided additional evidence, obtained through comprehensive analyses of entire animals at the single-cellular level and in greater sample sizes, to support the model that proposes distinctive growth patterns for different populations of neurons during regeneration.

## Fine network of planarian musculature and distinct intersections at head-tail poles

Motivated by the crucial function of muscle in regeneration and the need to comprehend the control of movement by the neuromuscular system, we investigated the interaction between the neuronal and muscular systems. Initially, we examined the distribution of musculature in planarians. The 6G10 antibody was used to visualize the distribution of muscles throughout the planarian (Cebrià, 2016 [DOI](#); Cote et al., 2019 [DOI](#)). Consequently, we validated that the body-wall musculature of adult planarians is composed of four layers of fibers, including circular, diagonal, longitudinal, dorsal-ventral (DV), and intestinal muscle fibers from the outmost to the innermost (Figure 4A [DOI](#), Figure S5A-D and J, Supplemental video 4).

With our higher-resolution images, we conducted segmentation to gain a better understanding of the organization and orientation of the muscle fibers (Figure 4B-H [DOI](#), Figure S5E-G, J, N). The planarian primarily relies on the movement of its cilia, which are mainly located on the ventral surface of the body (Rink et al., 2009 [DOI](#)). By closely examining the fiber structure, it becomes apparent that the circular muscle fibers dominate in all directions of the dorsal muscle wall (Figure 4C [DOI](#)). However, the ventral body-wall muscles contain a significant number of diagonal and longitudinal fibers at the tail region (Figure 4C [DOI](#)). In contrast, the proportion of these fibers decreases in the dorsal muscle wall (Figure 4C [DOI](#)). DV fibers are shorter compared with other orientations fibers, and they often have branches instead of one single fiber (Figure 4F [DOI](#), Figure S5E-G). We observe that these DV fibers have close contact with diagonal and longitudinal fibers (Figure 4G, H [DOI](#), Figure S5G, M, N).

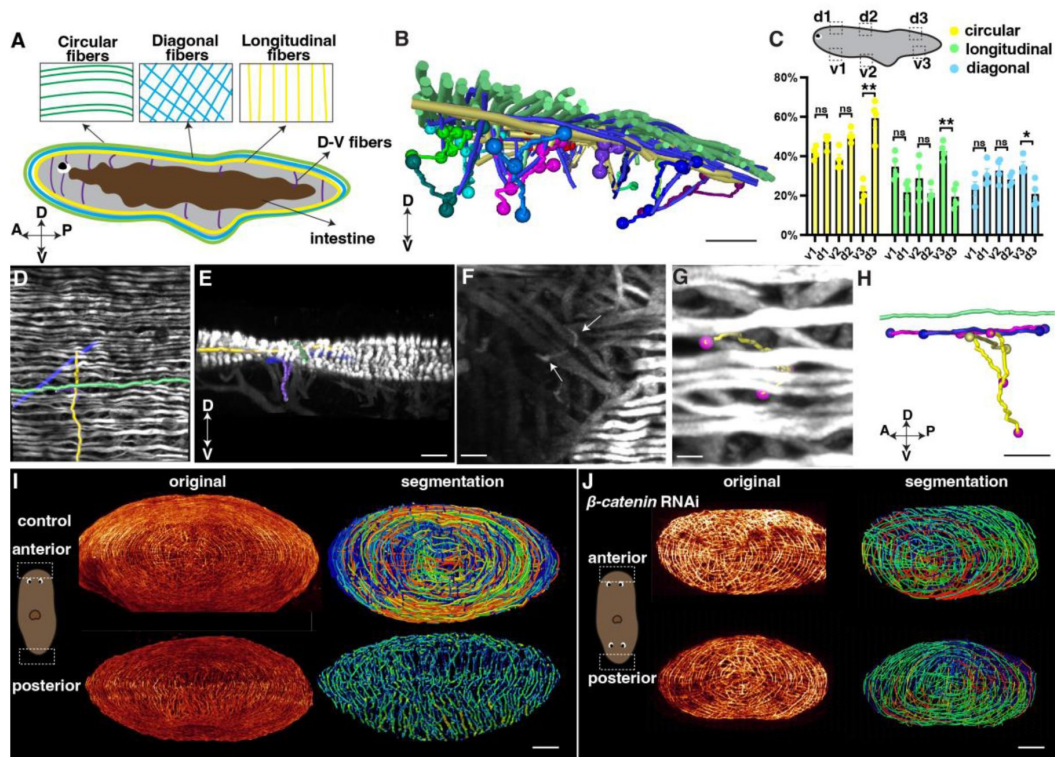


**Figure 4.**

Distribution of planarian body-wall muscle fibers and their connections at the anterior and posterior poles. **(A)** Illustration of the major five muscle fibers in wild-type planarians according to their orientation and distribution. A: anterior; P: posterior; D: dorsal; V: ventral. **(B)** Segmented fibers of planarian body-wall muscle. Scale bar, 200  $\mu$ m. **(C)** Schematic depicting selected segmented areas of planarian body-wall muscle, with a chart depicting the number of different orientational fibers in those regions. d: dorsal region; v: ventral region. The data is shown as the mean  $\pm$  SEM. Statistical significance was evaluated using the two-tailed unpaired Student's t-test, with \* $p < 0.05$ , \*\* $p < 0.01$ , \*\*\* $p < 0.001$  indicating significance, while ns indicates lack of significance. **(D)** Planarian dorsal body-wall muscle fiber labeled with 6G10 antibody staining, with segmented circular (green), diagonal (blue), longitudinal (yellow), and D-V fibers (purple). Scale bar, 150  $\mu$ m. **(E)** An xz view of the image in panel D. Scale bar, 150  $\mu$ m. **(F)** Selected 100  $\mu$ m depth region showing DV fiber (White arrows) located around diagonal fibers. Scale bar, 80  $\mu$ m. **(G)** Body-wall muscle fiber of a region in the image of panel F. Segmented D-V fibers are shown in a tracked line. Scale bar, 50  $\mu$ m. **(H)** An xz view of the segmented D-V fiber and its connecting fibers in panels F and G. Scale bar, 50  $\mu$ m. **(I)** Xz projection of planarian anterior and posterior muscle fiber and their segmented muscle fibers in control planarian. Scale bar, 300  $\mu$ m. **(J)** Xz projection of planarian anterior and posterior muscle fiber and their segmented muscle fibers in *β-catenin*-1 RNAi planarian. Scale bar, 300  $\mu$ m.

Internal organs, such as the eyes and intestine, consist of a sophisticated distribution of muscle fibers (Scimone et al., 2020 [DOI](#)). We were able to visualize the intricate musculature in these organs with a resolution of 120 nm. The eyes of planarians contain short, sparsely distributed muscle fibers (Figure S5H-J, Supplemental video 5). The pharynx, which serves as the feeding organ, is a muscular tube characterized by external and internal monostratified epithelia (Figure S5K, L). The intestine muscle fibers are located around the intestine, which are short and connected with small muscle fibers (Figure S5H-J). Furthermore, we investigated the connection between the dorsal epidermis and pharynx. We found that DV muscle fibers extend from the diagonal and circular layers of the dorsal body-wall muscles and connect with the longitudinal fibers of the pharynx (Figure S5M, N, Supplemental video 6). These observations suggest that the planarian musculature is an interconnected unit, with the internal tissue muscles connected to the external body-wall muscles.

Through the 3D tissue reconstruction method, we validated that the dorsal and ventral muscle fibers combine with circular muscle fibres, resembling in a cobweb-like structure in the anterior pole (Miller and Newmark, 2012 [DOI](#)). Moreover, we observed that the integration of the ventral and dorsal body wall muscles differs in the anterior and posterior regions of the body. In the posterior region, the dorsal and ventral muscle walls integrate differently with longitudinal muscle fibers (Figure 4I [DOI](#), Supplemental videos 7 and 8). It raised the possibility of whether the different morphologies are related to the A-P polarity. We thus examined the muscle structure at both the anterior and posterior heads of  $\beta$ -catenin-1 RNAi planarians. Both the anterior and posterior muscle fibers of  $\beta$ -catenin-1 RNAi planarians resemble the cobweb-like structure (Figure 4J [DOI](#)). These detailed structures suggest a correlation between muscle structure and the establishment of the anterior-posterior axis. The results highlight a noticeable contrast between the muscle fiber patterning of head and tail regions in terms of their responses to targets and adjustments in body posture. Unlike the tail, which doesn't need to react as actively, the head requires rapid reactions and precise posture changes. This is reflected in the more intricate muscle fiber arrangements observed in the head, suggesting a greater requirement for neural control.

## Neural-muscular connection in planarian homeostasis and regeneration

We next observed the interaction between neuronal and muscular networks. The *estrella*<sup>+</sup> glial cells are widespread (Figure 5A1-A3 [DOI](#)), and the glial cells extend from the planarian CNS to the body-wall muscle fibers (Figure 5A4, A5 [DOI](#)). On closer examination of the epidermis region, we observed a tight association between glial cells and muscle fibers (Figure 5 [DOI](#) 1-3, Supplemental video 9). We further investigated the neuronal and muscular connection through dual staining of 6G10 antibody (muscles) and anti-Phospho (Ser/Thr) (Figure 5B1-B3 [DOI](#)) or anti-SYT (neurons) (Figure 5C1, C2 [DOI](#)). Both dual-labeling revealed that neural cells are closely associated with muscle fibers with their projections (Figure 5B [DOI](#) 4-B6, C3-C5).

In the context of planarian regeneration, the expression of positional control genes (PCGs) by muscles is vital for orchestrating the complex process of tissue regrowth. During the regeneration process, DV muscles initially regenerate into longitudinal fibers at the anterior tip and later integrate with circular and diagonal fibers through small DV fiber branches (Figure S5O1-O3). By visualizing the dual-staining of cholinergic neurons and muscle fibers, we can observe that cholinergic neurons are closely located to muscle fibers from day 0 (Figure S5P1). We found that the appearance of newly regenerated diagonal and circular muscle fibers is located closely with cholinergic neurons (Figure S5P2, P3). These results suggest that the newly formed muscle fibers organize and connect potentially with a strong correlation with CNS.



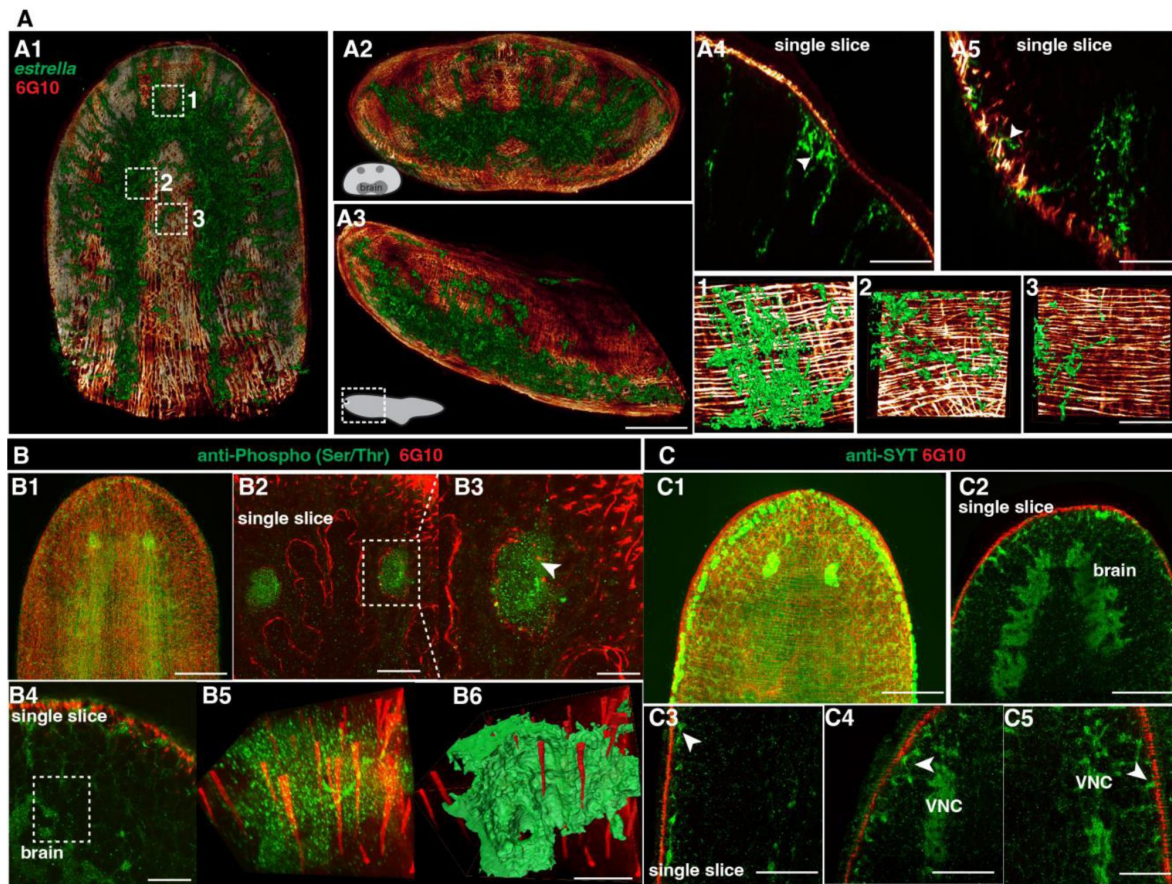


**Figure 5.**

Spatial connection of planarian neurons and glial cells with muscle fibers. **(A1)** Dual staining for glial cells (*estrella*<sup>+</sup>) and muscles (6G10<sup>+</sup>) in a wild-type planarian. The representative brain region of xy is shown. **(A2)** Dual staining for glial cells (*estrella*<sup>+</sup>) and muscles (6G10<sup>+</sup>) in a wild-type planarian. The representative brain region of xz is shown. **(A3)** Dual staining for glial cells (*estrella*<sup>+</sup>) and muscles (6G10<sup>+</sup>) in a wild-type planarian. The representative brain region of yz is shown. Scale bar, 600  $\mu$ m. **(A4)** A single slice of glial cells (*estrella*<sup>+</sup>) and muscles (6G10<sup>+</sup>) close to the epidermis of the anterior pole is shown. The arrowhead indicates the interaction of glial cells (*estrella*<sup>+</sup>) and muscles (6G10<sup>+</sup>). Scale bar, 250  $\mu$ m. **(A5)** A single slice of glial cells (*estrella*<sup>+</sup>) and muscles (6G10<sup>+</sup>) close to the epidermis of the posterior pole is shown. The arrowhead indicates the interaction of glial cells (*estrella*<sup>+</sup>) and muscles (6G10<sup>+</sup>). Scale bar, 250  $\mu$ m. **(1-3)** Zoomed in white dotted box region in A1 showing the *estrella*<sup>+</sup> glial projection to the muscles. Scale bar, 150  $\mu$ m. **(B1)** Dual staining for CNS (Anti-Phospho (Ser/Thr) staining) and muscles (6G10<sup>+</sup>) in a wild-type planarian. Scale bar, 600  $\mu$ m. **(B2)** Single slice of anti-Phospho (Ser/Thr) and 6G10 expression around planarian's eye. Scale bar, 300  $\mu$ m. **(B3)** Magnification of selected region in panel B2. Scale bar, 200  $\mu$ m. **(B4)** Single slice of Anti-Phospho (Ser/Thr) and 6G10 staining in a brain region. Scale bar, 200  $\mu$ m. **(B5)** Volume rendering of selected region in panel B4. **(B6)** Reconstruction of B5. Scale bar, 60  $\mu$ m. **(C1)** Dual staining for CNS (anti-SYT staining) and muscles (6G10<sup>+</sup>) in a wild-type planarian. Scale bar, 600  $\mu$ m. **(C2)** Single slice of Anti-SYT and 6G10 expression in brain region. Scale bar, 600  $\mu$ m. **(C3)** Single slice of Anti-SYT and 6G10 expression close to the epidermis in the middle part of the body. Scale bar, 450  $\mu$ m. **(C4)** Single slice of Anti-SYT and 6G10 expression close to the epidermis in the anterior part of the body. Scale bar, 450  $\mu$ m. **(C5)** Single slice of Anti-SYT and 6G10 expression close to the epidermis in the anterior part of the body. Scale bar, 450  $\mu$ m.



## Muscular infrastructure may support as a scaffold for the neuron projection

To further investigate the functional relationship between neuronal and muscular networks, we utilized previously reported gene RNAi strategy (Roberts-Galbraith, 2022 [DOI](#)) that are likely to impact the structures of muscle. Insulin may have an influence on the proper signaling of skeletal muscles and neoblasts (Miller and Newmark, 2012 [DOI](#); Lei et al., 2016 [DOI](#); Sylow et al., 2021 [DOI](#)). *Inr-1* RNAi animals exhibited locomotion defects (Lei et al., 2016 [DOI](#)) and also display a higher length-to-width ratio compared to control animals (Figure S6A, Supplemental video 10), suggesting possible neuromuscular system abnormalities. The body wall muscle fiber distribution in *inr-1* RNAi and  $\beta$ -catenin-1 RNAi planarians differs from *egfp* RNAi planarians (Figure 6A, B [DOI](#)). By calculating the concentration of different orientations of muscle fibers in *inr-1* RNAi and  $\beta$ -catenin-1 RNAi planarians in a  $500 \times 250 \times 300 \mu\text{m}^3$  region (Figure 6C [DOI](#)), we noticed that *inr-1* RNAi planarian has more circular fibers in both dorsal and ventral regions;  $\beta$ -catenin-1 RNAi planarian has more longitudinal fibers in dorsal regions (Figure 6C [DOI](#)).

Furthermore, an examination of sub-cellular neuronal expression is conducted using FISH labeling to identify cholinergic, dopaminergic, serotonergic, octopaminergic, GABAergic neurons, and glial cells (Figure S6B, C). *Inr-1* RNAi planarians manifested fewer cholinergic neurons and less glial branching in the brain region (Figure S6B, C). The distribution of GABAergic neurons was disordered in *inr-1* RNAi planarians (Figure S6B). Enhancement of muscle fibers revealed a substantial increase in the concentration of circular muscle fibers in both the ventral and dorsal regions (Figure 6A-C [DOI](#), Figure S6D). These results imply that the decreased presence of neurons and unusual arrangement of fibers with varying orientations within the body muscle wall may lead to locomotion impairments in *inr-1* RNAi planarians.

Considering that glial cell guidance is necessary for proper muscle fiber branching, the localization of *estrella*<sup>+</sup> glia and muscle fibers is further investigated. By dual-staining of anti-Phospho (Ser/Thr) and 6G10 in *inr-1* RNAi and  $\beta$ -catenin-1 RNAi planarians, we found that the morphologies of neurons are normal, and they have close contact with muscle fibers (Figure 6D, E [DOI](#)). However, by dual staining of *estrella* and 6G10, we found that the structure of glial cells is star-shaped in *egfp* RNAi planarian, however glial cells in *inr-1* RNAi and  $\beta$ -catenin-1 RNAi planarians have shorter cytoplasmic projections, and their sizes are smaller, lacking the major projection onto the muscles (Figure 6D, E [DOI](#), Figure S6E-K). Especially, in the posterior head of  $\beta$ -catenin-1 RNAi planarians, the glial cell has few axons and can hardly connect with muscle fibers (Figure 6E [DOI](#)). These results indicated that proper neuronal guidance and muscle fiber distribution could potentially contribute to facilitating accurate glial-to-muscle projections.

## Discussion

In this study, we employed TLSM and C-MAP to investigate the spatial organization in planarians at the single-cell level. Our findings provide valuable insights into the cellular composition and neuronal diversity of planarians, shedding light on their regenerative capabilities and the interactions between muscle fibers and neurons during the regeneration process. One of the key observations in our study was the development of a robust segmentation method that allowed for the accurate identification and characterization of individual cells throughout the planarian body. This segmentation method, combined with the application of tissue expansion techniques, provided an accessible approach to obtaining high-resolution spatial information and enabled us to obtain a comprehensive view of the cellular landscape. Through the application of a 3D tissue reconstruction method, we investigated the development and diversity of various neuron types, including cholinergic, GABAergic, octopaminergic, dopaminergic, and serotonergic neurons, at the single-cell level. In addition, we pay attention to the neural networks of the planarian visual

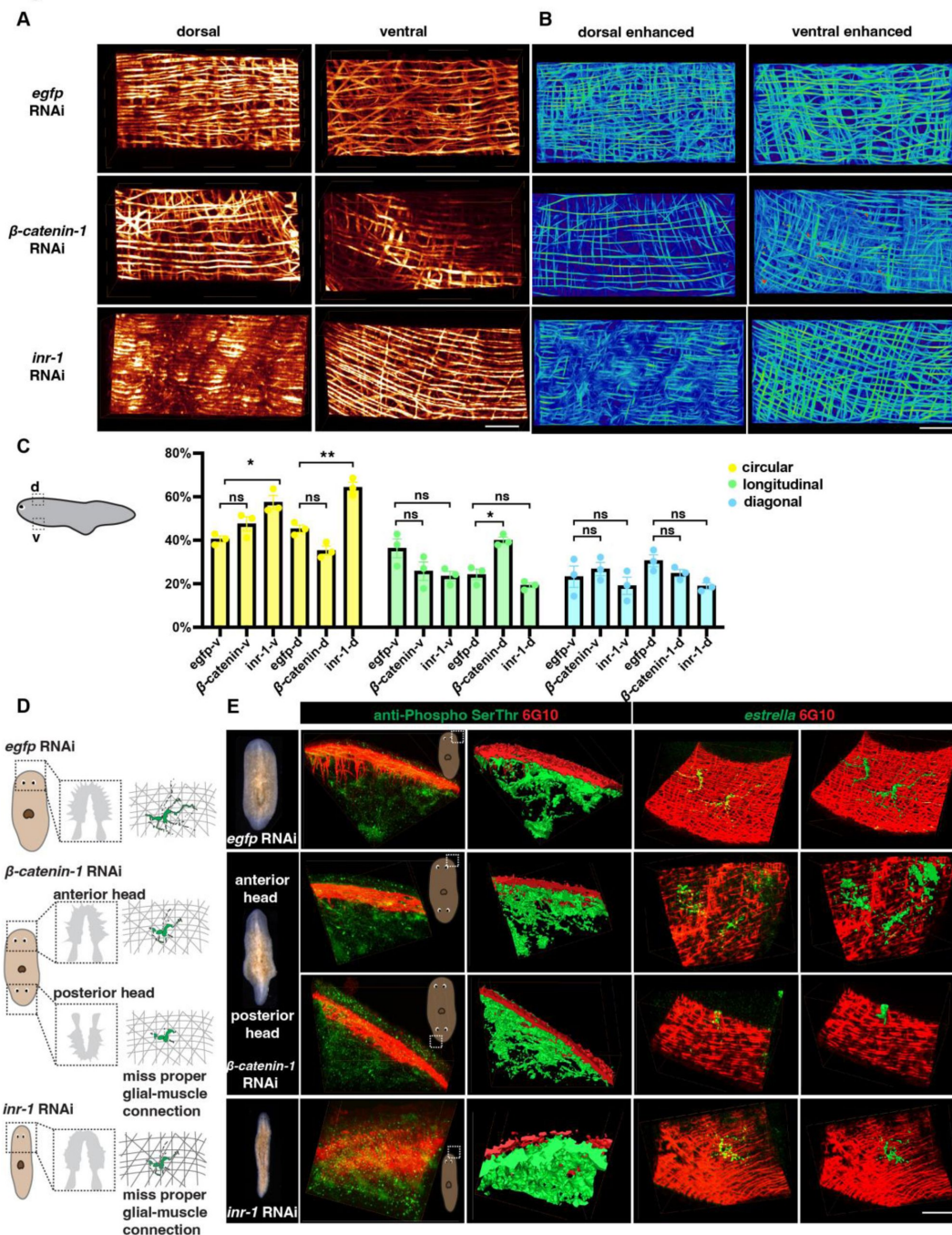


**Figure 6.**

Neuron and muscle defects in *inr-1* RNAi and  $\beta$ -*catenin* RNAi planarians (**A**) Representative images of dorsal and ventral muscle in *egfp* RNAi, *inr-1* RNAi, and  $\beta$ -*catenin-1* RNAi planarians. Scale bar, 120  $\mu$ m. (**B**) Images depicting enhanced muscle fibers within dorsal and ventral regions of *egfp* RNAi, *inr-1* RNAi, and  $\beta$ -*catenin-1* RNAi planarian. Scale bar, 40  $\mu$ m. (**C**) Schematic depicting selected segmented areas of planarian body-wall muscle in DV view. The plot shows the proportion of circular, longitudinal, and diagonal fibers in ventral and dorsal body muscle wall in *egfp* RNAi, *inr-1* RNAi, and  $\beta$ -*catenin-1* RNAi planarians. The data is shown as the mean  $\pm$  SEM. Statistical significance was evaluated using the two-tailed unpaired Student's t-test, with \* $p < 0.05$ , \*\* $p < 0.01$ , \*\*\* $p < 0.001$  indicating significance, while ns indicates lack of significance. (**D**) Illustration of *egfp* RNAi, *inr-1* RNAi, and  $\beta$ -*catenin-1* RNAi planarian glial cell structure and its connection with muscle fibers. (**E**) Anti-Phospho (Ser/Thr) and 6G10 expression and its reconstructed data in selected regions of *egfp* RNAi, *inr-1* RNAi, and  $\beta$ -*catenin-1* RNAi planarians (left). The *estrella*<sup>+</sup> glia and 6G10<sup>+</sup> muscles and their reconstructed images in selected regions of *egfp* RNAi, *inr-1* RNAi, and  $\beta$ -*catenin-1* RNAi planarians (right). Scale bar, 150  $\mu$ m.

system, and we validated that there are contralateral axon projections onto the brain with single axon tracing results. Our analysis unveiled the intricate distribution of neurons throughout the planarian nervous system, encompassing regions such as the brain, ventral nerve cords, optic, and pharyngeal nerve complex.

Notably, as the planarian's body size increased, we observed that all neuron subtypes exhibited growth alongside the body cells, consistent with previous reports (Takeda et al., 2009 [DOI](#); Arnold et al., 2019 [DOI](#); Oviedo et al., 2003 [DOI](#)). Multiple approaches were used and validated to study the planarian cell changes (Thommen et al., 2019 [DOI](#); Oviedo et al., 2003 [DOI](#); Hill et al., 2015). It is worth noticing that until reaching a threshold, beyond which the proportion of neurons decreases. This intriguing observation suggests a correlation with planarian fission, where the reduction in neuron proportion may be associated with the division of the planarian into two separate individuals. Our findings suggest that different neuron populations have coinciding regeneration speeds, and even the same neuron population may separate into different regeneration groups. Further investigations into the molecular and cellular mechanisms underlying this phenomenon would provide deeper insights into the factors governing planarian fission and the regenerative capacities of these organisms.

An important aspect of our study was the exploration of the interaction between muscle fibers and neurons during the regeneration process. By examining the structure, location, and regeneration of muscle fibers, as well as their connections to cholinergic neurons and glial cells labeled with *estrella*, we discovered a close correlation between ventral muscle fibers in the inner epidermal layer and cholinergic neurons and glial cytoplasmic projections. This finding suggests that muscle may play a crucial role in guiding the regeneration of the planarian nervous system, laying the foundation for future investigations into the neuron and muscle regeneration dynamics. Furthermore, 3D tissue imaging offers several advantages for clinical research and the medical industry by enhancing diagnostic accuracy through improved spatial resolution. Notably, techniques such as light sheet microscopy and tissue clearing have shown their utility in visualizing human tissues, as well as mouse tissues and various other model animals (Chung et al., 2013 [DOI](#); Liebmann et al., 2016 [DOI](#); Liu et al., 2016 [DOI](#)). The integration of two modalities, TLSM and C-MAP, allows for effective 3D imaging with a resolution range of 120 nm to 500 nm. We envision opportunities to expand our efforts to include additional research organisms, such as axolotls, hydra, and frogs, thereby broadening the scope of our research.

In conclusion, our study utilizing tiling light-sheet microscopy and C-MAP expansion techniques provides a comprehensive understanding of planarian spatial organization and cellular dynamics at the single-cell level. The development of a robust segmentation method, combined with the analysis of various neuron types and their relationship with muscle fibers, highlights the intricate interactions between different cell populations during planarian regeneration. These findings significantly contribute to our knowledge of regenerative biology and provide a foundation for future studies to understand similar processes in other organisms. Further investigations into the functional significance of the observed cellular dynamics and interactions will undoubtedly advance our understanding of planarian biology and regenerative mechanisms.

## Materials and methods

## Key resources table

REAGENT or RESOURCE	SOURCE	IDENTIFIER
<b>Antibodies</b>		
Anti-Digoxigenin (DIG)-POD	Roche	11207733910
Anti-Fluorescein-POD	Roche	11426346910
6G10	DSHB	6G10-2C7
Anti-Arrestin	Takeshi Inuo	
Anti-SYT	Takeshi Inuo	
<b>Bacterial and virus strains</b>		
<i>Escherichia coli</i> DH5a	N/A	N/A
<i>Escherichia coli</i> HT115	N/A	N/A
<b>Chemicals</b>		
urea	Sangon	A600148
N-butyl diethanolamine	TCL chemicals	#B0725
Triton X-100	SIGMA	T8787-250ml
Tween20	SIGMA	P9416-100ml
methanol	SCR	80080418
Acrylamide	Sangon	A100341
N,N-Dimethylacrylamide	SigmaAldrich	M7279
Sodium acrylate	Macklin	S833838
2,2'-Azobis[2-(2-imidazolin-2-yl) propane] dihydrochloride (VA-044)	Rhawn	R008695
Formaldehyde	SIGMA	F8775
Heparin	SIGMA	H3149
Torula Yeast RNA	SIGMA	R6625
Western Blocking Reagent	Roche	11921681001
Horse Serum	hyclone	N/A
Dextran Sulfate	Sangon	A600160
Maleic acid	aladdin	M108866
NAC	SIGMA	A7250
DAPI	Thermo Scientific	FisherD3306
Phusion High-Fidelity DNA Polymerase	NEB	M0530L
T7 RNA Polymerase	Promega	P207E
MicroSpin G-50 Columns	Cytiva	27533002
StarPrep Gel Extraction Kit	GenStar	D205-04
FsatPure Plasmid Mini Kit	Vazyme	DC201-01
DIG RNA Labeling Mix	Roche	11277073910
Fluorescein RNA Labeling Mix	Roche	11685619910
DNase (RQ1 rnase free DNase)	Promega	PAM 6101
anti-Phospho (Ser/Thr)	CST	9631S
<b>Software</b>		
Amira 3D	Thermo Scientific	Fisher2023

<b>Organism</b>		
<i>Schmidtea mediterranea</i> , asexual	N/A	CIW4
<b>Other</b>		
hybridization oven	xingfen	FYY-3
Thermocycler	Analytik Jena	Biometra TRIO 48
Microscope Cameras	Leica	DFC7000 T



## Data and code availability

The analyzed data, the recipe files, and the processed data of the nuclei segmentation, neuron segmentation, and muscle fiber segmentation have been deposited to the open external repository Zenodo (<https://zenodo.org/>), including the files listed below.

1. Planarian cell counting recipe: <https://zenodo.org/records/11724834/files/planarianCellCounting.hxrecipe?download=1>
2. Planarian cell counting project file: <https://zenodo.org/records/11724834/files/planarian%20nuclei%20cell%20counting.togo?download=1>
3. Planarian neuron counting recipe: <https://zenodo.org/records/11724834/files/planarianNeuronCellCounting.hxrecipe?download=1>
4. Planarian neuron counting project file: <https://zenodo.org/records/11724834/files/planarian%20neuron%20cell%20counting.togo?download=1>
5. Planarian allometry measure recipe <https://zenodo.org/records/11724834/files/planarianAllometryMeasure.hxrecipe?download=1>
6. Planarian allometry measure project file: <https://zenodo.org/records/11724834/files/planarianallometrymeasure.togo?download=1>
7. Planarian anterior muscle segmentation project file: <https://zenodo.org/records/11724834/files/planarianAnteriorMuscleSegmentation.togo?download=1>
8. Planarian posterior muscle segmentation project file: <https://zenodo.org/records/11724834/files/planarianPosteriorMuscleSegmentation.togo?download=1>
9. Planarian nuclei data (labeled with PI): <https://zenodo.org/records/11724834/files/planarianNucleiGrayscale.togo?download=1>
10. Planarian musculature data (labeled with 6G10): <https://zenodo.org/records/12533272>

The raw data for statistical analysis in each figure have been provided in this paper as source data, which include source data of **fig 2**, **fig 3**, **fig 4**, **fig 6**, and fig S1, S3, S4, S6.

The details of the protocols are described in the following Methods. Requests for further information about the methodologies and resources are available upon request to the corresponding authors, Kai Lei ([leikai@westlake.edu.cn](mailto:leikai@westlake.edu.cn)) and Liang Gao ([gaoliang@westlake.edu.cn](mailto:gaoliang@westlake.edu.cn)).

## Planarian culture and amputation

*Schmidtea mediterranea* clonal asexual strain CIW4 animals were maintained in 1× Montjuic salts (1.6 mmol/L NaCl, 1.0 mmol/L CaCl<sub>2</sub>, 1.0 mmol/L MgSO<sub>4</sub>, 0.1 mmol/L MgCl<sub>2</sub>, 0.1 mmol/L KCl and 1.2 mmol/L NaHCO<sub>3</sub> prepared in Milli-Q water) at 20°C as previously described (Cebrià and Newmark, 2005), and were fed with liver paste every three days. Intact animals (1–14 mm in length) were starved for at least 7 days before each experiment. The worms (5–6 mm long) were amputated into two sections: anterior fragment (including pharynx) and tail.

## In situ hybridization and immunostaining

Fluorescence in situ hybridization was performed as previously described (King and Newmark, 2013). Intact and regeneration samples were treated with reduction solution (1% v/v NP-40, 0.5% w/v SDS, and 50 mM DTT in 1×PBS) for 10 min at 37 °C, except for worms within 3 days post-amputation, and all samples were bleached with Ryan King's Bleach (5% Formamide, 1.2% H<sub>2</sub>O<sub>2</sub> in 0.5× SSC) for 2 hours. Riboprobes were synthesized as previously described (King and Newmark, 2013). The primers are as follows: *Smed-chat* (SMED30031525) forward primer 5'-CTTTGGCACTTCGATAAAC-3', reverse primer 5'-CCATTCTGTGTGTCGATTGG-3'; *Smed-gad* (SMED30001003) forward primer 5'-TATCAAAATAGGTCAGGGCC-3', reverse primer 5'-AAACGCCGCCATCTAATTTC-3'; *Smed-tbh* (SMED30017498) forward primer 5'-

TTGGTCTGTTGAACCGAATC-3', reverse primer 5'-AATCTCCCTCAAAAGAGTCG-3'; *Smed-th* (SMED30012000) forward primer 5'-CACCAGTCAGAAATTCATCG-3', reverse primer 5'-TATCATGAAAACCCGGATGG-3'; *Smed-tph* (SMED30012020) forward primer 5'-ACCAGACGAGGAAGATTTTC-3', reverse primer 5'-GCAAGACCAGCTAAAAAGTC-3'; *Smed-estrella* (KY024338.1) forward primer 5'-CAAATGCTGAGAATACTGGC-3', reverse primer 5'-TCGGAGTAAGCATCGTTTAG-3'. Animals were incubated with probes labeled with DIG (1:500) for more than 18h at 56°C. Anti-DIG-POD 1:1000 (Roche) was used in MABT containing 5% Horse Serum and 0.5% Roche Western Blocking Reagent. The antibody 6G10 (1:1000, DSHB) was used in PBSTB (PBSTx 0.1%+ 1% Bovine Serum Albumin [Jackson Immuno Research Laboratories]) for FISH. For anti-DIG-POD labeling, samples were incubated overnight at 4°C and then developed with FITC-conjugated tyramide (1:2000) in borate buffer containing 0.006% H<sub>2</sub>O<sub>2</sub> for 1 hour at room temperature. For dual staining with antibodies, the worms were overnight incubated at 4°C with 6G10 (1:1000), followed by incubation with the secondary antibody Goat Anti-mouse IgG H&L (HRP) pre-adsorbed (1:1000 in PBSTx0.3%, Abcam) on the following day. Subsequently, the worms were incubated with rhodamine-tyramide (1:5000) in borate buffer containing 0.006% H<sub>2</sub>O<sub>2</sub> for 1 hour on the third day. The same procedure was repeated for the additional antibody staining, including anti-arrestin (rabbit, 1:500), anti-SYT (rabbit, 1:1100), and anti-Phospho (Ser/Thr) (rabbit, 1:1000).

## Tissue clearing for planarians

Tissue clearing was performed following the CUBIC protocol ([Matsumoto et al., 2019](#)), with specific optimizations for the planarian sample. The tissue-clearing solution consisted of 15% urea, 10% N-butyl diethanolamine, 10% Triton X-100, and 65% deionized water (ddH<sub>2</sub>O). The specimens were immersed in this solution and gently shaken at either room temperature or 37°C.

The duration of tissue clearing varied depending on the size and starvation state of the planarians, ranging from 30 minutes to overnight. It is worth noting that excessively long tissue clearing can compromise the integrity of planarian tissues. Starved planarians measuring 2-3 mm should skip the tissue-clearing step and proceed directly to the expansion procedure. Conversely, tail fragments that have been amputated from a 6 mm planarian require the tissue-clearing step.

For planarians of different sizes and developmental stages, the tissue clearing time should be adjusted based on their starvation status. An extended period of starvation allows for a reduction in tissue clearing time.

## C-MAP for planarians

The planarian specimen should be washed with 0.01 M PBS for 30 minutes at room temperature, with gentle shaking to ensure thorough clearance. To prepare the monomer solution, the final concentrations of the components should be as follows: 30% Acrylamide (AA), 0.075% N, N-Dimethylacrylamide (BA), 10% Sodium acrylate (SA), and 0.5% 2,2'-Azobis[2-(2-imidazolin-2-yl)propane] dihydrochloride (VA-044) in 0.01 M PBS. It is important to store the monomer solution at 4°C and use it within 7 days.

Next, the planarian specimen should be immersed in the monomer solution for 30 minutes at 4°C. The length of monomer incubation may vary depending on the size of the planarians, ranging from 30 minutes to overnight. For planarian of 2 mm length, the monomer incubation time is 30 minutes.

To perform the gelation step, it is necessary to work on ice. To create a double-layer gel that prevents direct contact between the specimen and the mold surface, start by adding 200 µL of the monomer solution onto the cap of a 1.5 mL Eppendorf (EP) tube on ice. Make sure that no sample

is included in this first layer. The polymerization is initiated by exposing the gel to ultraviolet (UV) light for approximately 5 seconds, resulting in the formation of a coagulated gel with a tacky surface for support.

Afterward, carefully pipette the planarian specimen and 250  $\mu\text{L}$  of monomer solution onto the first gel layer. This second layer should be solidified using UV light for 30 seconds, with the light source positioned 15 cm away from the sample. It is important not to use UV light to check the sample's position until it is properly placed in the mold. Once the specimen is embedded in the gel, separate the gel containing the specimen from the EP tube cap using tweezers and transfer it to ddH<sub>2</sub>O in a 10 cm Corning cell culture plate. The specimen should be stored at room temperature for 2 days, with the ddH<sub>2</sub>O changed after overnight incubation. Gentle shaking can be applied to expedite the expansion process.

To further increase the expansion ratio, the monomer solution should have the following final concentrations: 30% Acrylamide (AA), 0.05% N, N-Dimethylacrylamide (BA), 10% Sodium acrylate (SA), and 0.5% 2,2'-Azobis[2-(2-imidazolin-2-yl)propane] dihydrochloride (VA-044) in 0.01 M PBS.

## Labeling of planarian nuclei

After an overnight expansion, the gel underwent a two-fold increase in size. To achieve accurate results, carefully use a blade accompanied by an illuminating light to precisely section the gel. These incisions should be in accordance with the contour of the planarian specimen, resulting in a cuboid shape. Subsequently, immerse the trimmed gel once again in fresh ddH<sub>2</sub>O supplemented with 0.50  $\mu\text{g/mL}$  of Propidium Iodide (PI) for nuclei staining at room temperature with gentle shaking. Stain the planarian overnight and wash the sample with ddH<sub>2</sub>O for 10 minutes before imaging.

## Sample mounting

The planarian specimen, which had been embedded within the gel, was carefully trimmed with a blade to achieve a flat bottom surface. Following this, the gel was affixed onto a thin magnet using adhesive glue. The magnet's dimensions were modifiable to align with the sample's proportions. Lastly, the gel-magnet assembly was secured onto a designated sample holder prepared for imaging.

## Imaging

The configuration and operational details of the microscope were described in earlier publications (Chen et al., 2020 [DOI](#); Feng et al., 2021 [DOI](#)). Employing distinct arrangements of light sheet configuration and detective objectives, the expanded planarian specimen was subjected to imaging for specific experiment purposes. The planarians labeled with nuclei and neuron pool were imaged with OLYMPUS MV PLAPO 1 $\times$  objective with micron-scale spatial resolution. The planarians labeled with 6G10 and *estrella* were imaged with OLYMPUS 10 $\times$ 0.6 SV MP to achieve sub-micron spatial resolution. The resolution can be up to  $\sim 70 \times 70 \times 210 \text{ nm}^3$  with this combination of objective and tilling light sheets. The image processing, registration, and merging procedure was described in detail in a previous publication (Chen et al., 2020 [DOI](#)).

## Resolution calculation

For cellular resolution imaging, we utilized a 1 $\times$  air objective with a numerical aperture (NA) of 0.25 and a working distance of 60 mm (OLYMPUS MV PLAPO). The voxel size used was  $0.8 \times 0.8 \times 2.5 \text{ }\mu\text{m}^3$ . This configuration resulted in a resolution of  $2 \times 2 \times 5 \text{ }\mu\text{m}^3$  and a spatial resolution of  $0.5 \times 0.5 \times 1.25 \text{ }\mu\text{m}^3$  with 4 $\times$  isotropic expansion. Alternatively, for sub-cellular imaging, we employed a 10 $\times$ 0.6 SV MP water immersion objective with 0.8 NA and a working distance of 8 mm

(OLYMPUS). The voxel size used in this configuration was  $0.26 \times 0.26 \times 0.8 \mu\text{m}^3$ . As a result of this configuration, we achieved a resolution of  $0.5 \times 0.5 \times 1.6 \mu\text{m}^3$  and a spatial resolution of  $0.12 \times 0.12 \times 0.4 \mu\text{m}^3$  with a  $4.5\times$  isotropic expansion.

## RNAi interference

*egfp*, without nucleotide sequence homology in planarians, was used as control RNAi. Animals were fed 1-6 times bacterially colored food (90% liver, 5.5% water containing  $1\times$  Montjuic salts with 4.5% red food coloring)-expressed *egfp*, *smed-inr-1*,  $\beta$ -catenin, and *egfr-3* double-stranded RNA, once every 3 days. Animals were fixed 7 days after the last feeding.

## Nuclei quantification

The cellular quantification workflow was developed using the Amira 3D software environment (<https://www.thermofisher.com/software-em-3d-vis/customerportal/download-center/amira-avizo-3d-installers/>). A recipe and an example for nuclei counting can be assessed from <https://zenodo.org/records/11724834>. This recipe is designed for the segmentation of planarian nuclei-labeled images. The image analysis modules in the recipe provide flexibility for users to interactively check results at each step. Modules such as interactive thresholding and structure enhancement filters are designated as check breakpoints for parameter adjustment. The workflow consists of the following steps:

1. Use the volume edit module to eliminate the noise and irrelevant signals in the background. Select the noise or overexposed small objects using the lasso tool or handle box.
2. Apply either the Anisotropic diffusion or Gaussian filter to process the volumetric data. In the volume edit module, divide the planarian into two parts (the head and the remaining regions) using the lasso tool. Use the segmentation editor to visualize the original image and the selection. Annotate regions for addition or deletion using the brush tool, and speed up the process using the interpolate function. Check the selected data using xy, yz, xz views, and 3D renderings
3. Smooth the data use either a Gaussian filter or anisotropic diffusion filter. In this workflow, we use an additional built-in Python script to enhance the nuclei edges and remove the noise.
4. To further enhance the visualization of cellular structures and cell boundaries, a 3D structure enhancement filter module was implemented. The 3D Hessian ball recognition port was selected to match the circular structure while removing others. This step is set as a breakpoint in the recipe and the standard deviation port can be adjusted to match the data structure. In the workflow for the head region, the standard deviation min/max pixel parameters were set as 1 and 6, respectively, with the standard deviation step of 1. In other body parts, the standard deviation min/max pixel parameters were set as 1 and 3, respectively, with a standard deviation step of 1. The ball recognition in the 3D structure enhancement module was used to detect cell edges. Alternatively, the 2D Hessian tensor was selected for cell edges or background boundary detection. The standard deviation min/max pixels ports were both set as 1, and the standard deviation step was set as 1.
5. Transform the grayscale image into a binary image using an interactive thresholding module. Adjust the threshold of binary pixels using an ortho slice of the original image and the binary signals until they match. This step is identified as a breakpoint in the recipe, and the threshold value can be adjusted on a case-by-case basis.
6. Apply the “remove small spots” module to eliminate smaller objects of noise or background.
7. Use either the watershed segmentation or marker-based watershed segmentation modules to label individual neurons and demarcate their separation. Attach the segmentation function to label the results of cells and background. Check the segmentation results in the segmentation editor.



8. Finally, manual examination was performed slice by slice in segmentation editor to correct mis-segmentation or over-segmentation.

## Neuron quantification

The recipe of neuron counting and an example can be freely accessed from <https://zenodo.org/records/11724834>. The workflow used for quantifying neurons closely resembled that of nuclei quantification, with two important considerations. First, due to the sparser distribution of neurons compared to somatic cells, the overall neuron data can be analyzed without the need to distinguish between the brain and other regions. Second, adjustments were made to the minimum and maximum parameters of the structure enhancement function standard deviation based on the staining size of the neuronal markers. The workflow can be broken down into the following steps.

1. Anisotropic diffusion or Gaussian filter was employed initially to reduce the noise and smooth the data.
2. A structure enhancement filter was then used to enhance the neuron signals. This step is set as a breakpoint in the recipe, and the standard deviation port can be adjusted to match the data structure. In our example, the standard deviation was set to a minimum of 2 pixels and an maximum of 5 pixels, respectively, with a step size of 1.
3. Apply interactive thresholding module to transform the grayscale volumetric image into binary image. The threshold of binary pixels was adjusted using an ortho slice of the original image and the binary signals until they align. The interactive thresholding function is marked as a breakpoint in the recipe, and the threshold value can be adjusted on a case-by-case basis. The remove small spots module was then employed to remove small objects below a certain pixel value.
4. Finally, the labelling module was used to assign labels to each neuron. The labelling function was linked to cell and cell boundary results. The recipe was designed for use with neuron pool labeling datasets, and careful parameter adjustments at breakpoints are recommended.

## Measurement of planarian length and volume

The recipe and an example of measuring volumetric parameters can be freely accessed from <https://zenodo.org/records/11724834>. The workflow can be broken down into the following steps.

1. Due to the large data size, it is necessary to apply the resampling function to reduce the volumetric planarian nuclei data below 1 GB to make it suitable for GPU computation.
2. Anisotropic diffusion should be implemented to decrease the sharp edges in both the signal and background of the planarian specimen, while preserving the external contour. To achieve this, it is recommended to increase the threshold of anisotropic diffusion and the number of iterations to smooth the data.
3. An interactive thresholding module should be executed to convert the grayscale image into a binary image. Adjust the threshold of binary pixels can be done by utilizing an ortho slice of the original image and the binary signals until they match.
4. After completing the transformation, it is crucial to apply a fill small holes module to mitigate any voids present within the particles.
5. To resolve uneven surface contours, the compute ambient occlusion algorithm module was utilized to calculate an ambient occlusion scalar field for the dataset. It is advised to increase the maximum distance value and the number of rays to further smooth the data.
6. The segmented portion and the padded region were integrated using an arithmetic algorithm.

7. Subsequently, a label analysis module, along with 3D measurements, was applied to determine notable metrics such as the length and volume of an expanded planarian.

## Neuron tracing

Single anti-arrestin labelled neuron tracing analysis was conducted with Amira 3D filament editor. Initially, 10 to 50 single-layer images were selected for maximum intensity projection display, based on their grayscale signals. Next, we identified and selected the axons to be tracked by determining their starting and ending points. Subsequently, layers were selected for display using the maximum intensity projection method. This approach facilitated the segmental tracking of the main axon, as well as the identification of branching points, thereby enabling the comprehensive tracking of neural fibers in 3D. Following the completion of the fiber tracking, we conducted a validation process to assess the accuracy of the traced fibers by comparing them with the original single-layer images. This validation was performed in multiple directions, with different branches of the fibers displayed in distinct colors.

To render the anti-SYT, anti-Phospho (Ser/Thr), *estrella*, and anti-arrestin labelled data, we utilized Amira 3D segmentation editor. First, the datasets were transformed from grayscale to binary using interactive thresholding. Subsequently, the mis-segmented areas were evaluated and corrected using either the brush tool or lasso tool. Lastly, the data was displayed using either volume rendering or the surface module generation method.

## Muscle fiber tracing

The muscle fiber tracing workflow was developed using Amira 3D. The data and project file related to muscle fiber tracing can be freely accessed from <https://zenodo.org/records/11724834>. The workflow can be broken down into the following steps.

1. The fiber data set was initially processed with the unsharp 3D masking module. This module was used to enhance the clarity of fiber edges without introducing additional noise.
2. The structure enhancement filter was implemented to extract the inherent fiber characteristics. The standard deviation min/max pixels were both set to 1, with a standard deviation step of 1 in the rod recognition structure type.
3. After enhancement of the structure, we utilized the cylinder correlation module to identify the fiber location and orientation by specifying parameters such as the fiber length, inner diameter, and outer diameter of the target cylinder. For anterior planarian muscle segmentation scenario, we set cylinder length to 18, the angular sampling to 5, the mask cylinder radius to 3, and the outer cylinder radius to 2.8. Note that these parameters may vary with other datasets.
4. The fluorescent signals conforming to the cylindrical shape were isolated and enhanced using the cylinder correlation module. The trace correlation line module was then utilized to extract and locate the target fibers. The output from this module was visualized with a spatial graph, providing key parameters and detailed information about traced fiber length and orientation.

## Statistical Analyses

Microsoft Excel and Prism 9 were used for statistical analysis. The data in all graphs are shown as the mean  $\pm$  SEM. An unpaired two-tailed Student's *t*-test was used to determine the significance of differences between the two conditions. Differences for which  $P < 0.05$  were considered statistically significant.

## Acknowledgements

We thank all laboratory members for their constructive comments. K.L. is supported by the National Natural Science Foundation of China (32122032, 31970750), the "Pioneer" and "Leading Goose" R&D Program of Zhejiang (2024SSYS0030), Zhejiang Provincial Key Laboratory Construction Project, and the Westlake Education Foundation. L.G. is supported by the Zhejiang Province Natural Science Foundation (LR20C070002) and the Westlake Education Foundation.

## Author contributions

Conceptualization: J.L., H.X., L.G. and K.L.; methodology: J.L., H.X., L.G. and K.L.; investigation: J.L., H.X., D.W., Y.C. and T. I.; visualization: J.L.; funding acquisition: L.G. and K.L.; project administration: L.G. and K.L.; supervision: L.G. and K.L.; writing – original draft: J.L. and K.L.; writing – review & editing: J.L., H.X., T.I., L.G. and K.L.

## Competing interests

Multiple patents regarding the described light sheet microscopy and tissue expansion techniques were filed by Westlake University on behalf of the authors.

**Supplemental video 1.** Examples of cell segmentation in planarians after ETLSM.

**Supplemental video 2.** 3D images of the five major neuron types in planarians.

**Supplemental video 3.** 3D image of the visual projections in a wild-type planarian.

**Supplemental video 4.** 3D image of the body-wall muscle on the surface of a wild-type planarian.

**Supplemental video 5.** 3D view of muscle fibers surrounding the planarian eyes.

**Supplemental video 6.** 3D view of DV muscles connecting the body-wall muscles and the pharyngeal muscles.

**Supplemental video 7.** 3D view of muscle interconnection at the anterior pole of a wild-type planarian.

**Supplemental video 8.** 3D view of muscle interconnection at the posterior pole of a wild-type planarian.

**Supplemental video 9.** 3D view of glial cell projection onto the body-wall muscles.

**Supplemental video 10.** Swimming behavior of *inr-1* RNAi and *egfp* RNAi planarians.

## References

- Agata K., Soejima Y., Kato K., Kobayashi C., Umesono Y., Watanabe K (1998) **Structure of the planarian central nervous system (CNS) revealed by neuronal cell markers** *Zoological science* **15**:433–440 <https://doi.org/10.2108/zsj.15.433>
- Arnold C.P., Benham-Pyle B.W., Lange J.J., Wood C.J., Sanchez Alvarado A (2019) **Wnt and TGFbeta coordinate growth and patterning to regulate size-dependent behaviour** *Nature* **572**:655–659 <https://doi.org/10.1038/s41586-019-1478-7>
- Bullock T., Horridge G.A (1965) **Structure and function in the nervous systems of invertebrates** *Freeman: San Francisco*
- Cajal S.R (1995) **Histology of the Nervous System of Man and Vertebrates** Oxford Univ Press
- Cebrià F (2007) **Regenerating the central nervous system: how easy for planarians!** *Dev Genes Evol* **217**:733–748 <https://doi.org/10.1007/s00427-007-0188-6>
- Cebrià F (2016) **Planarian Body-Wall Muscle: Regeneration and Function beyond a Simple Skeletal Support** *Front Cell Dev Biol* **4** <https://doi.org/10.3389/fcell.2016.00008>
- Cebrià F., Newmark P.A (2005) **Planarian homologs of netrin and netrin receptor are required for proper regeneration of the central nervous system and the maintenance of nervous system architecture** *Development* **132**:3691–3703 <https://doi.org/10.1242/dev.01941>
- Cebrià F., Nakazawa M., Mineta K., Ikeo K., Gojobori T., Agata K (2002) **Dissecting planarian central nervous system regeneration by the expression of neural-specific genes** *Dev Growth Differ* **44**:135–146 <https://doi.org/10.1046/j.1440-169x.2002.00629.x>
- Chandra B., Voas M.G., Davies E.L., Roberts-Galbraith R.H (2023) **Ets-1 transcription factor regulates glial cell regeneration and function in planarians** *Development* **150** <https://doi.org/10.1242/dev.201666>
- Chang J.B. *et al.* (2017) **Iterative expansion microscopy** *Nat Methods* **14**:593–599 <https://doi.org/10.1038/nmeth.4261>
- Chen F., Tillberg P.W., Boyden E.S (2015) **Optical imaging. Expansion microscopy** *Science* **347**:543–548 <https://doi.org/10.1126/science.1260088>
- Chen Y. *et al.* (2020) **A Versatile Tiling Light Sheet Microscope for Imaging of Cleared Tissues** *Cell Rep* **33** <https://doi.org/10.1016/j.celrep.2020.108349>
- Chung K. *et al.* (2013) **Structural and molecular interrogation of intact biological systems** *Nature* **497**:332–337 <https://doi.org/10.1038/nature12107>
- Cote L.E., Simental E., Reddien P.W (2019) **Muscle functions as a connective tissue and source of extracellular matrix in planarians** *Nat Commun* **10** <https://doi.org/10.1038/s41467-019-09539-6>



- Currie K.W., Molinaro A.M., Pearson B.J (2016) **Neuronal sources of hedgehog modulate neurogenesis in the adult planarian brain** *Elife* 5 <https://doi.org/10.7554/eLife.19735>
- Dotd H.U., Leischner U., Schierloh A., Jahrling N., Mauch C.P., Deininger K., Deussing J.M., Eder M., Zieglgansberger W., Becker K (2007) **Ultramicroscopy: three-dimensional visualization of neuronal networks in the whole mouse brain** *Nat Methods* 4:331–336 <https://doi.org/10.1038/nmeth1036>
- Eisenhoffer G.T., Kang H., Sánchez Alvarado A (2008) **Molecular analysis of stem cells and their descendants during cell turnover and regeneration in the planarian *Schmidtea mediterranea*** *Cell Stem Cell* 3:327–339 <https://doi.org/10.1016/j.stem.2008.07.002>
- Feng R., Wang D., Chen Y., Lu J., Gao L (2021) **Protocol for constructing a versatile tiling light sheet microscope for imaging cleared tissues** *STAR Protoc* 2 <https://doi.org/10.1016/j.xpro.2021.100546>
- Fu Q., Martin B.L., Matus D.Q., Gao L (2016) **Imaging multicellular specimens with real-time optimized tiling light-sheet selective plane illumination microscopy** *Nat Commun* 7 <https://doi.org/10.1038/ncomms11088>
- Gao L (2015) **Extend the field of view of selective plan illumination microscopy by tiling the excitation light sheet** *Opt Express* 23:6102–6111 <https://doi.org/10.1364/OE.23.006102>
- Gao R. *et al.* (2019) **Cortical column and whole-brain imaging with molecular contrast and nanoscale resolution** *Science* 363 <https://doi.org/10.1126/science.aau8302>
- Hill E.M., Petersen C.P (2015) **Wnt/Notum spatial feedback inhibition controls neoblast differentiation to regulate reversible growth of the planarian brain** *Development* 142:4217–4229 <https://doi.org/10.1242/dev.123612>
- Matsumoto K. *et al.* (2019) **Advanced CUBIC tissue clearing for whole-organ cell profiling** *Nat Protoc* 14:3506–3537 <https://doi.org/10.1038/s41596-019-0240-9>
- Khariton M., Kong X., Qin J., Wang B (2020) **Chromatic neuronal jamming in a primitive brain** *Nat Phys* 16:553–557 <https://doi.org/10.1038/s41567-020-0809-9>
- King R.S., Newmark P.A (2013) **In situ hybridization protocol for enhanced detection of gene expression in the planarian *Schmidtea mediterranea*** *BMC Dev Biol* 13 <https://doi.org/10.1186/1471-213X-13-8>
- Ku T., Swaney J., Park J.Y., Albanese A., Murray E., Cho J.H., Park Y.G., Mangena V., Chen J., Chung K (2016) **Multiplexed and scalable super-resolution imaging of three-dimensional protein localization in size-adjustable tissues** *Nat Biotechnol* 34:973–981 <https://doi.org/10.1038/nbt.3641>
- Lei K., Thi-Kim Vu H., Mohan R.D., McKinney S.A., Seidel C.W., Alexander R., Gotting K., Workman J.L., Sánchez Alvarado A (2016) **Egf Signaling Directs Neoblast Repopulation by Regulating Asymmetric Cell Division in Planarians** *Dev Cell* 38:413–429 <https://doi.org/10.1016/j.devcel.2016.07.012>
- Li D.J., McMan C.L., Reddien P.W (2019) **Nuclear receptor NR4A is required for patterning at the ends of the planarian anterior-posterior axis** *Elife* 8 <https://doi.org/10.7554/eLife.42015>

- Liebmann T., Renier N., Bettayeb K., Greengard P., Tessier-Lavigne M., Flajolet M (2016) **Three-Dimensional Study of Alzheimer's Disease Hallmarks Using the iDISCO Clearing Method** *Cell Rep* **16**:1138–1152 <https://doi.org/10.1016/j.celrep.2016.06.060>
- Liu A.K., Hurry M.E., Ng O.T., DeFelice J., Lai H.M., Pearce R.K., Wong G.T., Chang R.C., Gentleman S.M (2016) **Bringing CLARITY to the human brain: visualization of Lewy pathology in three dimensions** *Neuropathol Appl Neurobiol* **42**:573–587 <https://doi.org/10.1111/nan.12293>
- Miller C.M., Newmark P.A (2012) **An insulin-like peptide regulates size and adult stem cells in planarians** *The International journal of developmental biology* <https://doi.org/10.1387/ijdb.113443cm>
- Nishimura K., Kitamura Y., Umesono Y., Takeuchi K., Takata K., Taniguchi T., Agata K (2008) **Identification of glutamic acid decarboxylase gene and distribution of GABAergic nervous system in the planarian Dugesia japonica** *Neuroscience* **153**:1103–1114 <https://doi.org/10.1016/j.neuroscience.2008.03.026>
- Obernier K., Tong C.K., Alvarez-Buylla A (2014) **Restricted nature of adult neural stem cells: re-evaluation of their potential for brain repair** *Front Neurosci* **8** <https://doi.org/10.3389/fnins.2014.00162>
- Oviedo N.J., Newmark P.A., Sánchez Alvarado A (2003) **Allometric scaling and proportion regulation in the freshwater planarian Schmidtea mediterranea** *Dev Dyn* **226**:326–333 <https://doi.org/10.1002/dvdy.10228>
- Pearson B.J., Eisenhoffer G.T., Gurley K.A., Rink J.C., Miller D.E., Sánchez Alvarado A (2009) **Formaldehyde-based whole-mount in situ hybridization method for planarians** *Dev Dyn* **238**:443–450 <https://doi.org/10.1002/dvdy.21849>
- Rink J.C., Gurley K.A., Elliott S.A., Sánchez Alvarado A (2009) **Planarian Hh signaling regulates regeneration polarity and links Hh pathway evolution to cilia** *Science* **326**:1406–1410 <https://doi.org/10.1126/science.1178712>
- Roberts-Galbraith R.H (2022) **RNAi Screening to Assess Tissue Regeneration in Planarians** *Methods Mol Biol* **2450**:509–527 [https://doi.org/10.1007/978-1-0716-2172-1\\_27](https://doi.org/10.1007/978-1-0716-2172-1_27)
- Roberts-Galbraith R.H., Brubacher J.L., Newmark P.A (2016) **A functional genomics screen in planarians reveals regulators of whole-brain regeneration** *Elife* **5** <https://doi.org/10.7554/eLife.17002>
- Scimone M.L., Atabay K.D., Fincher C.T., Bonneau A.R., Li D.J., Reddien P.W (2020) **Muscle and neuronal guidepost-like cells facilitate planarian visual system regeneration** *Science* **368** <https://doi.org/10.1126/science.aba3203>
- Syrow L., Tokarz V.L., Richter E.A., Klip A (2021) **The many actions of insulin in skeletal muscle, the paramount tissue determining glycemia** *Cell Metab* **33**:758–780 <https://doi.org/10.1016/j.cmet.2021.03.020>
- Takeda H., Nishimura K., Agata K (2009) **Planarians maintain a constant ratio of different cell types during changes in body size by using the stem cell system** *Zoological science* **26**:805–813 <https://doi.org/10.2108/zsj.26.805>

Thommen A. *et al.* (2019) **Body size-dependent energy storage causes Kleiber's law scaling of the metabolic rate in planarians** *Elife* 8 <https://doi.org/10.7554/eLife.38187>

Tillberg P.W. *et al.* (2016) **Protein-retention expansion microscopy of cells and tissues labeled using standard fluorescent proteins and antibodies** *Nat Biotechnol* 34:987–992 <https://doi.org/10.1038/nbt.3625>

Tomer R., Khairy K., Keller P.J (2011) **Shedding light on the system: studying embryonic development with light sheet microscopy** *Curr Opin Genet Dev* 21:558–565 <https://doi.org/10.1016/j.gde.2011.07.003>

Umesono Y., Agata K (2009) **Evolution and regeneration of the planarian central nervous system** *Dev Growth Differ* 51:185–195 <https://doi.org/10.1111/j.1440-169X.2009.01099.x>

Wang I.E., Lapan S.W., Scimone M.L., Clandinin T.R., Reddien P.W (2016) **Hedgehog signaling regulates gene expression in planarian glia** *Elife* 5 <https://doi.org/10.7554/eLife.16996>

Wassie A.T., Zhao Y., Boyden E.S (2019) **Expansion microscopy: principles and uses in biological research** *Nat Methods* 16:33–41 <https://doi.org/10.1038/s41592-018-0219-4>

Xie J., Feng R., Chen Y., Gao L (2023) **Morphological analysis of descending tracts in mouse spinal cord using tissue clearing, tissue expansion and tiling light sheet microscopy techniques** *Sci Rep* 13 <https://doi.org/10.1038/s41598-023-43610-z>

## Editors

Reviewing Editor

**Frank Chan**

University of Groningen, Groningen, Netherlands

Senior Editor

**Christopher Huang**

University of Cambridge, Cambridge, United Kingdom

## Reviewer #1 (Public review):

Summary:

The planarian flatworm *Schmidtea mediterranea* is widely used as a model system for regeneration because of its remarkable ability to regenerate its entire body plan from very small fragments of tissue, including the complete and rapid regeneration of the CNS. Prior to this study, analysis of CNS regeneration in planaria has mostly been performed on a gross anatomical level. Despite its simplicity compared to vertebrates, the CNS of many invertebrates, including planaria, is nonetheless complex, intricate, and densely packed. Some invertebrate models allow the visualization of individual cellular components of the CNS using transgenic techniques. Until transgenesis becomes commonplace in planaria, the visualization and analysis of detailed CNS anatomy must rely on alternate approaches in order to capitalize on the immense promise of this system as a model for CNS regeneration. Another challenge for the study of the CNS more broadly is how to perform imaging of a complete CNS on a reasonable timescale such that multiple individuals per experimental condition can be imaged.

Strengths:

In this report, Lu et al. describe a careful and detailed analysis of the planarian neuroanatomy and musculature in both the homeostatic and regenerating contexts. To improve the effective resolution of their imaging, the authors optimized a tissue expansion protocol for planaria. Imaging was performed by light sheet microscopy, and the resulting optical sections were tiled to reconstruct whole worms. Labelled tissues and cells were then segmented to allow quantification of neurons and muscle fibers, as well as all cells in individual worms using a DNA dye. The resulting workflow can produce highly detailed and quantifiable 3D reconstructions at a rate that is fast enough to allow the analysis of large numbers of animals.

#### Weaknesses:

Lu et al. use their workflow to visualize RNA expression of five enzymes that are each involved in the biosynthetic pathway of different neurotransmitters/modulators, namely chat (cholinergic), gad (GABAergic), tbh (octopaminergic), th (dopaminergic), and tph (serotonergic). In this way, they generate an anatomical atlas of neurons that produce these molecules. Collectively these markers are referred to as the "neuronpool." They overstate when they write, "The combination of these five types of neurons constitutes a neuron pool that enables the labeling of all neurons throughout the entire body." This statement does not accurately represent the state of our knowledge about the diversity of neurons in *S. mediterranea*. There are several lines of evidence that support the presence of glutamatergic and glycinergic neurons, including the following. The glutamate receptor agonists NMDA and AMPA both produce seizure-like behaviors in *S. mediterranea* that are blocked by the application of glutamate receptor antagonists MK-801 and DNQX (which antagonize NMDA and AMPA glutamate receptors, respectively; Rawls et al., 2009). scRNA-Seq data indicates that neurons in *S. mediterranea* express a vesicular glutamate transporter, a kainite-type glutamate receptor, a glycine receptor, and a glycine transporter (Brunet Avalos and Sprecher, 2021; Wyss et al., 2022). Two AMPA glutamate receptors, GluR1 and GluR2, are known to be expressed in the CNS of another planarian species, *D. japonica* (Cebria et al., 2002). Likewise, there is abundant evidence for the presence of peptidergic neurons in *S. mediterranea* (Collins et al., 2010; Fraguas et al., 2012; Ong et al., 2016; Wyss et al., 2022; among others) and in *D. japonica* (Shimoyama et al., 2016). For these reasons, the authors should not assume that all neurons can be assayed using the five markers that they selected. The situation is made more complex by the fact that many neurons in *S. mediterranea* appear to produce more than one neurotransmitter/modulator/peptide (Brunet Avalos and Sprecher, 2021; Wyss et al., 2022), which is common among animals (Vaaga et al., 2014; Brunet Avalos and Sprecher, 2021). However the published literature indicates that there are substantial populations of glutamatergic, glycinergic, and peptidergic neurons in *S. mediterranea* that do not produce other classes of neurotransmission molecule (Brunet Avalos and Sprecher, 2021; Wyss et al., 2022). Thus it seems likely that the neuronpool will miss many neurons that only produce glutamate, glycine or a neuropeptide.

The authors use their technique to image the neural network of the CNS using antibodies raised vs. Arrestin, Synaptotagmin, and phospho-Ser/Thr. They document examples of both contralateral and ipsilateral projections from the eyes to the brain in the optic chiasma (Figure 1C-F). These data all seem to be drawn from a single animal in which there appears to be a greater than normal number of nerve fiber defasciculations. It isn't clear how well their technique works for fibers that remain within a nerve tract or the brain. The markers used to image neural networks are broadly expressed, and it's possible that most nerve fibers are too densely packed (even after expansion) to allow for image segmentation. The authors also show a close association between estrella-positive glial cells and nerve fibers in the optic chiasma.

The authors count all cell types, neuron pool neurons, and neurons of each class assayed. They find that the cell number to body volume ratio remains stable during homeostasis



(Figure S3C), and that the brain volume steadily increases with increasing body volume (Figure S3E). They also observe that the proportion of neurons to total body cells is higher in worms 2-6 mm in length than in worms 7-9 mm in length (Figure 2D, S3F). They find that the rate at which four classes of neurons (GABAergic, octopaminergic, dopaminergic, serotonergic) increase relative to the total body cell number is constant (Figure S3G-J). They write: "Since the pattern of cholinergic neurons is the major cell population in the brain, these results suggest that the above observation of the non-linear dynamics between neurons and cell numbers is likely from the cholinergic neurons." This conclusion should not be reached without first directly counting the number of cholinergic neurons and total body cells. Given that glutamatergic, glycinergic, and peptidergic neurons were not counted, it also remains possible that the non-linear dynamics are due (in part or in whole) to one or more of these populations.

The authors next assayed the production of different classes of neurons in regenerating post-pharyngeal tail fragments. At 14 dpa, they find significantly reduced proportions of octopaminergic, GABAergic, and dopaminergic neurons in these regenerated animals (Figure 3K). Given that these three neuron classes are primarily found in the brain region (Figure S2A), this suggests that the brains of these animals may not have finished regenerating by 14 dpa.

The authors next applied their imaging and segmentation technique to the musculature using the 6G10 antibody. They find that the body wall muscle fibers from the dorsal and ventral body walls integrate differently at the anterior end (to form a cobweb-like arrangement) compared to the posterior end (Figure 4I). They knock down  $\beta$ -catenin in regenerating head anterior fragments and find that the resulting double-headed worms produce a cobweb-like arrangement at both ends (Figure 4J).

RNAi knockdown of *inr-1* is known to produce mobility defects and have elongated bodies relative to control animals (Lei et al., 2016; Figure S6A). To understand the nature of these defects, the authors image the muscle of *inr-1* RNAi animals and find increased circular body wall muscle fibers on both dorsal and ventral sides, while  $\beta$ -catenin RNAi animals have increased longitudinal muscle fibers on the dorsal side (Figure 6C). The *inr-1* RNAi animals also have reduced cholinergic neurons (Figure S6B), and ectopic expression of the GABAergic marker *gad* in the periphery (Figure S6B). Lastly the authors simultaneously image muscle and estrellin-positive glia and find that these glia lack their typically elaborate stellate morphology in *inr-1* RNAi animals (Figure 6E, S6E-K). The combination of this muscle, neuronal, and glial defects may account for the mobility defects observed in *inr-1* RNAi worms.

<https://doi.org/10.7554/eLife.101103.1.sa3>

## Reviewer #2 (Public review):

### Summary:

This manuscript builds on the authors' 2020 study by combining tissue expansion with light sheet microscopy to quantify the organism-wide spatial distribution of various cell types in the planarian.

### Strengths:

- (1) The quantification of cell types as a function of animal size and regeneration stages could be a useful resource for the planarian research community.
- (2) The high-quality images can help clarify some anatomical structures within the planarian tissues.

#### Weaknesses:

- (1) The proprietary nature of the microscope, protected by a patent, limits the technical details provided, making the method hard to reproduce in other labs.
- (2) The resolution of the analyses is mostly limited to the cellular level, which does not fully leverage the advantages of expansion microscopy. Previous applications of expansion microscopy have revealed finer nanostructures in the planarian nervous system (see Fan et al. *Methods in Cell Biology* 2021; Wang et al. *eLife* 2021). It is unclear whether the current protocol can achieve a comparable resolution.
- (3) The data largely corroborate past observations, while the novel claims are insufficiently substantiated.

#### A few major issues with the claims:

- (4) Line 303-304: While 6G10 is a widely used antibody to label muscle fibers in the planarian, it doesn't uniformly mark all muscle types (Scimone et al. *Nature* 2017). For a more complete view of muscle fibers, it is important to use a combination of antibodies targeting different fiber types or a generic marker such as phalloidin. This raises fundamental concerns about all the conclusions drawn from Figures 4 and 6 about differences between various muscle types. Additionally, the authors should cite the original paper that developed the 6G10 antibody (Ross et al. *BMC Developmental Biology* 2015).
- (5) Lines 371-379: The claim that DV muscles regenerate into longitudinal fibers lacks evidence. Furthermore, previous studies have shown that TFs specifying different muscle types (DV, circular, longitudinal, and intestinal) both during regeneration and homeostasis are completely different (Scimone et al., *Nature* 2017 and Scimone et al., *Current Biology* 2018). Single-cell RNAseq data further establishes the existence of divergent muscle progenitors giving rise to different muscle fibers. These observations directly contradict the authors' claim, which is only based on images of fixed samples at a coarse time resolution.
- (6) Line 423: The manuscript lacks evidence to claim glia guide muscle fiber branching.
- (7) Lines 432/478: The conclusion about neuronal and muscle guidance on glial projections is similarly speculative, lacking functional evidence. It is possible that the morphological defects of *estrella*<sup>+</sup> cells after *bcat1* RNAi are caused by Wnt signaling directly acting on *estrella*<sup>+</sup> cells independent of muscles or neurons.
- (8) Finally, several technical issues make the results difficult to interpret. For example, in line 125, cell boundaries appear to be determined using nucleus images; in line 136, the current resolution seems insufficient to reliably trace neural connections, at least based on the images presented.

<https://doi.org/10.7554/eLife.101103.1.sa2>

#### Reviewer #3 (Public review):

##### Summary:

In this manuscript, the authors apply tissue expansion and tiling light sheet microscopy to study allometric growth and regeneration in planaria. They developed image analysis pipelines to help them quantify different neuronal subtypes and muscles in planaria of different sizes and during regeneration. Among the strengths of this work, the authors provide beautiful images that show the potential of the approaches they are taking and their ability to quantify specific cell types in relatively large numbers of whole animal samples.

Many of their findings confirm previous results in the literature, which helps validate the techniques and pipelines they have applied here. Among their new observations, they find that the body wall muscles at the anterior and posterior poles of the worm are organized differently and show that the muscle pattern in the posterior head of beta-catenin RNAi worms resembles the anterior muscle pattern. They also show that glial cell processes appear to be altered in beta-catenin or insulin receptor-1 RNAi worms. Weaknesses include some over-interpretation of the data and lack of consideration or citation of relevant previous literature, as discussed below.

#### Strengths:

This method of tissue expansion will be useful for researchers interested in studying this experimental animal. The authors provide high-quality images that show the utility of this technique. Their analysis pipeline permits them to quantify cell types in relatively large numbers of whole animal samples.

The authors provide convincing data on changes in total neurons and neuronal sub-types in different-sized planaria. They report differences in body wall muscle pattern between the anterior and posterior poles of the planaria, and that these differences are lost when a posterior head forms in beta-catenin RNAi planaria. They also find that glial cell projections are reduced in insulin receptor-1 RNAi planaria.

#### Weaknesses:

The work would have been strengthened by a more careful consideration of previous literature. Many papers directly relevant to this work were not cited. Such omissions do the authors a disservice because in some cases, they fail to consider relevant information that impacts the choice of reagents they have used or the conclusions they are drawing.

For example, when describing the antibody they use to label muscles (monoclonal 6G10), they do not cite the paper that generated this reagent (Ross et al PMID: PMC4307677), and instead, one of the papers they do cite (Cebria 2016) that does not mention this antibody. Ross et al reported that 6G10 does not label all body wall muscles equivalently, but rather "predominantly labels circular and diagonal fibers" (which is apparent in Figure S5A-D of the manuscript being reviewed here). For this reason, the authors of the paper showing different body wall muscle populations play different roles in body patterning (Scimone et al 2017, PMID: PMC6263039, also not cited in this paper) used this monoclonal in combination with a polyclonal antibody to label all body wall muscle types. Because their "pan-muscle" reagent does not label all muscle types equivalently, it calls into question their quantification of the different body wall muscle populations throughout the manuscript. It does not help matters that their initial description of the body wall muscle types fails to mention the layer of thin (inner) longitudinal muscles between the circular and diagonal muscles (Cebria 2016 and citations therein).

Ipsilateral and contralateral projections of the visual axons were beautifully shown by dye-tracing experiments (Okamoto et al 2005, PMID: 15930826). This paper should be cited when the authors report that they are corroborating the existence of ipsilateral and contralateral projections.

The proportional decrease of neurons with growth in *S. mediterranea* was shown by counting different cell types in macerated planarians (Baguna and Romero, 1981; <https://link.springer.com/article/10.1007/BF00026179>) and earlier histological observations cited there. These results have also been validated by single-cell sequencing (Emili et al, bioRxiv 2023, <https://www.biorxiv.org/content/10.1101/2023.11.01.565140v>). Allometric growth of the planaria tail (the tail is proportionately longer in large vs small planaria) can explain this decrease in animal size. The authors never really discuss allometric growth in a way that would help readers unfamiliar with the system understand this.

In some cases, the authors draw stronger conclusions than their results warrant. The authors claim that they are showing glial-muscle interactions, however, they do not provide any images of triple-stained samples labeling muscle, neurons, and glia, so it is impossible for the reader to judge whether the glial cells are interacting directly with body wall muscles or instead with the well-described submuscular nerve plexus. Their conclusion that neurons are unaffected by beta-cat or *inr-1* RNAi based on anti-phospho-Ser/Thr staining (Fig. 6E) is unconvincing. They claim that during regeneration "DV muscles initially regenerate into longitudinal fibers at the anterior tip" (line 373). They provide no evidence for such switching of muscle cell types, so it is unclear why they say this.

The authors show how their automated workflow compares to manual counts using PI-stained specimens (Figure S1T). I may have missed it, but I do not recall seeing a similar ground truth comparison for their muscle fiber counting workflow. I mention this because the segmented image of the posterior muscles in Figure 4I seems to be missing the vast majority of circular fibers visible to the naked eye in the original image.

It is unclear why the abstract says, "We found the rate of neuron cell proliferation tends to lag..." (line 25). The authors did not measure proliferation in this work and neurons do not proliferate in planaria.

It is unclear what readers are to make of the measurements of brain lobe angles. Why is this a useful measurement and what does it tell us?

The authors repeatedly say that this work lets them investigate planarians at the single-cell level, but they don't really make the case that they are seeing things that haven't already been described at the single-cell level using standard confocal microscopy.

<https://doi.org/10.7554/eLife.101103.1.sa1>

#### Author response:

##### **Reviewer #1 (Public review):**

*Lu et al. use their workflow to visualize RNA expression of five enzymes that are each involved in the biosynthetic pathway of different neurotransmitters/modulators, namely chat (cholinergic), gad (GABAergic), tbh (octopaminergic), th (dopaminergic), and tph (serotonergic). In this way, they generate an anatomical atlas of neurons that produce these molecules. Collectively these markers are referred to as the "neuronpool." They overstate when they write, "The combination of these five types of neurons constitutes a neuron pool that enables the labeling of all neurons throughout the entire body." This statement does not accurately represent the state of our knowledge about the diversity of neurons in *S. mediterranea*. There are several lines of evidence that support the presence of glutamatergic and glycinergic neurons, including the following. The glutamate receptor agonists NMDA and AMPA both produce seizure-like behaviors in *S. mediterranea* that are blocked by the application of glutamate receptor antagonists MK-801 and DNQX (which antagonize NMDA and AMPA glutamate receptors, respectively; Rawls et al., 2009). scRNA-Seq data indicates that neurons in *S. mediterranea* express a vesicular glutamate transporter, a kainite-type glutamate receptor, a glycine receptor, and a glycine transporter (Brunet Avalos and Sprecher, 2021; Wyss et al., 2022). Two AMPA glutamate receptors, GluR1 and GluR2, are known to be expressed in the CNS of another planarian species, *D. japonica* (Cebria et al., 2002). Likewise, there is abundant evidence for the presence of peptidergic neurons in *S. mediterranea* (Collins et al., 2010; Fraguas et al., 2012; Ong et al., 2016; Wyss et al., 2022; among others) and in *D. japonica* (Shimoyama et al., 2016). For these reasons, the authors should not assume that all*



*neurons can be assayed using the five markers that they selected. The situation is made more complex by the fact that many neurons in *S. mediterranea* appear to produce more than one neurotransmitter/modulator/peptide (Brunet Avalos and Sprecher, 2021; Wyss et al., 2022), which is common among animals (Vaaga et al., 2014; Brunet Avalos and Sprecher, 2021). However the published literature indicates that there are substantial populations of glutamatergic, glycinergic, and peptidergic neurons in *S. mediterranea* that do not produce other classes of neurotransmission molecule (Brunet Avalos and Sprecher, 2021; Wyss et al., 2022). Thus it seems likely that the neuronpool will miss many neurons that only produce glutamate, glycine or a neuropeptide.*

In response to your comments, we agree that our initial statement regarding the "neuron pool" overstated the extent of neuronal coverage provided by the five selected markers. We have revised the sentence as "The combination of these five types of neurons constitutes a neuron pool that enables the labeling of most of the neurons throughout the entire body, including the eyes, brain, and pharynx".

Furthermore, we chose the five neurotransmitter systems (cholinergic, GABAergic, octopaminergic, dopaminergic, and serotonergic) based on their well-characterized roles in planarian neurobiology and the availability of reliable markers. However, we acknowledge the limitations of this approach and recognize that it does not encompass all neuron types, particularly those involved in glutamatergic, glycinergic, and peptidergic signaling, which have been documented in *S. mediterranea*. We will also add the content about other neuron types in our revised manuscript "Additionally, there is considerable diversity among glutamatergic, glycinergic, and peptidergic neurons in planarians. Many neurons in *S. mediterranea* express more than one neurotransmitter or neuropeptide, which adds further complexity to the system."

*The authors use their technique to image the neural network of the CNS using antibodies raised vs. Arrestin, Synaptotagmin, and phospho-Ser/Thr. They document examples of both contralateral and ipsilateral projections from the eyes to the brain in the optic chiasma (Figure 1C-F). These data all seem to be drawn from a single animal in which there appears to be a greater than normal number of nerve fiber defasciculatations. It isn't clear how well their technique works for fibers that remain within a nerve tract or the brain. The markers used to image neural networks are broadly expressed, and it's possible that most nerve fibers are too densely packed (even after expansion) to allow for image segmentation. The authors also show a close association between estrella-positive glial cells and nerve fibers in the optic chiasma.*

Thank you for your detailed feedback. While we did not perform segmentation of all neuron fibers, we were able to segment more isolated fibers that were not densely packed within the neural tracts. We use 120 nm resolution to segment neurons along the three axes. Our data show the presence of both contralateral and ipsilateral projections of visual neurons. Although Figure 1C-F shows data from one planarian, we imaged three independent specimens to confirm the consistency of these observations. In the revised manuscript, we will include a discussion on the limitations of TLSM in reconstructing neural networks, particularly when it comes to resolving fibers within densely packed regions of the nerve tracts.

*The authors count all cell types, neuron pool neurons, and neurons of each class assayed. They find that the cell number to body volume ratio remains stable during homeostasis (Figure S3C), and that the brain volume steadily increases with increasing body volume (Figure S3E). They also observe that the proportion of neurons to total body cells is higher in worms 2-6 mm in length than in worms 7-9 mm in length (Figure 2D, S3F). They find that the rate at which four classes of neurons (GABAergic, octopaminergic,*

*dopaminergic, serotonergic) increase relative to the total body cell number is constant (Figure S3G-J). They write: "Since the pattern of cholinergic neurons is the major cell population in the brain, these results suggest that the above observation of the non-linear dynamics between neurons and cell numbers is likely from the cholinergic neurons." This conclusion should not be reached without first directly counting the number of cholinergic neurons and total body cells. Given that glutamatergic, glycinergic, and peptidergic neurons were not counted, it also remains possible that the non-linear dynamics are due (in part or in whole) to one or more of these populations.*

We have removed the statement "Since the pattern of cholinergic neurons is the major cell population in the brain, these results suggest that the above observation of the non-linear dynamics between neurons and cell numbers is likely from the cholinergic neurons." We changed this statement into "These results suggest that the above observation of the non-linear dynamics between neurons and cell numbers is not likely from the octopaminergic, GABAergic, dopaminergic and serotonergic neurons. Since our neuron pool may not include glutamatergic, glycinergic, and peptidergic neurons, we would like to add the possibility that the non-linear dynamics may be from cholinergic neurons or other neurons not included in our staining."

**Reviewer #2 (Public review):**

*Weaknesses:*

*(1) The proprietary nature of the microscope, protected by a patent, limits the technical details provided, making the method hard to reproduce in other labs.*

Thank you for your comment. We understand the importance of reproducibility and transparency in scientific research. We would like to point out that the detailed design and technical specifications of the TLSM are publicly available in our published work: Chen et al., Cell Reports, 2020. Additionally, the protocol for C-MAP, including the specific experimental steps, is comprehensively described in the methods section of this paper. We believe that these resources should provide sufficient information for other labs to replicate the method.

*(2) The resolution of the analyses is mostly limited to the cellular level, which does not fully leverage the advantages of expansion microscopy. Previous applications of expansion microscopy have revealed finer nanostructures in the planarian nervous system (see Fan et al. Methods in Cell Biology 2021; Wang et al. eLife 2021). It is unclear whether the current protocol can achieve a comparable resolution.*

Thank you for raising this important point. The strength of our C-MAP protocol lies in its fluorescence-protective nature and user convenience. Notably, the sample can be expanded up to 4.5-fold linearly without the need for heating or proteinase digestion, which helps preserve fluorescence signals. In addition, the entire expansion process can be completed within 48 hours. While our current analysis focused on cellular-level structures, our method can achieve comparable or better resolution and we will add this information in the revised manuscript.

*(3) The data largely corroborate past observations, while the novel claims are insufficiently substantiated.*

*A few major issues with the claims:*

*(4) Line 303-304: While 6G10 is a widely used antibody to label muscle fibers in the planarian, it doesn't uniformly mark all muscle types (Scimone et al. Nature 2017). For a more complete view of muscle fibers, it is important to use a combination of antibodies*

*targeting different fiber types or a generic marker such as phalloidin. This raises fundamental concerns about all the conclusions drawn from Figures 4 and 6 about differences between various muscle types. Additionally, the authors should cite the original paper that developed the 6G10 antibody (Ross et al. BMC Developmental Biology 2015).*

We appreciate the reviewer's insightful comments and acknowledge that 6G10 does not uniformly label all muscle fiber types. We agree that this limitation should be recognized in the interpretation of our results. We will revise the manuscript to explicitly state the limitations of using 6G10 alone for muscle fiber labeling and highlight the need for additional markers. We would also clarify that the primary objective of our study was not to distinguish all muscle fiber types but rather to demonstrate the application of our 3D tissue reconstruction method in addressing traditional research questions. Nonetheless, we agree that expanding the labeling strategy in future studies would allow for a more thorough investigation of muscle fiber diversity. We will ensure all citations are properly revised and updated in our next version.

*(5) Lines 371-379: The claim that DV muscles regenerate into longitudinal fibers lacks evidence. Furthermore, previous studies have shown that TFs specifying different muscle types (DV, circular, longitudinal, and intestinal) both during regeneration and homeostasis are completely different (Scimone et al., Nature 2017 and Scimone et al., Current Biology 2018). Single-cell RNAseq data further establishes the existence of divergent muscle progenitors giving rise to different muscle fibers. These observations directly contradict the authors' claim, which is only based on images of fixed samples at a coarse time resolution.*

Thank you for your valuable feedback. Our intent was not to suggest that DV muscles regenerate into longitudinal fibers. Our observations focused on the wound site, where DV muscle fibers appear to reconnect, and longitudinal fibers, along with other muscle types, gradually regenerate to restore the structure of the injured area. We will revise the relevant sections of the manuscript to clarify this dynamic process more accurately.

*(6) Line 423: The manuscript lacks evidence to claim glia guide muscle fiber branching.*

We will remove this statement from the revised version. Instead, we will focus on describing our observations of the connections between glial cells and muscle fibers.

*(7) Lines 432/478: The conclusion about neuronal and muscle guidance on glial projections is similarly speculative, lacking functional evidence. It is possible that the morphological defects of estrellas+ cells after bcat1 RNAi are caused by Wnt signaling directly acting on estrellas+ cells independent of muscles or neurons.*

We understand that this approach is insufficient and we will revise the manuscript to more clearly state the limitations of our data. We will describe our observations as preliminary and suggest that further experiments are required.

*(8) Finally, several technical issues make the results difficult to interpret. For example, in line 125, cell boundaries appear to be determined using nucleus images; in line 136, the current resolution seems insufficient to reliably trace neural connections, at least based on the images presented.*

We use two setups for imaging cells and neuron projections. For cellular resolution imaging, we utilized a 1× air objective with a numerical aperture (NA) of 0.25 and a working distance of 60 mm (OLYMPUS MV PLAPO). The voxel size used was 0.8×0.8×2.5 μm<sup>3</sup>. This configuration

resulted in a resolution of  $2 \times 2 \times 5 \mu\text{m}^3$  and a spatial resolution of  $0.5 \times 0.5 \times 1.25 \mu\text{m}^3$  with  $4 \times$  isotropic expansion. Alternatively, for sub-cellular imaging, we employed a  $10 \times 0.6$  SV MP water immersion objective with 0.8 NA and a working distance of 8 mm (OLYMPUS). The voxel size used in this configuration was  $0.26 \times 0.26 \times 0.8 \mu\text{m}^3$ . As a result of this configuration, we achieved a resolution of  $0.5 \times 0.5 \times 1.6 \mu\text{m}^3$  and a spatial resolution of  $0.12 \times 0.12 \times 0.4 \mu\text{m}^3$  with a  $4.5 \times$  isotropic expansion. The higher resolution achieved with sub-cellular imaging allows us to observe finer structures and trace neural connections.

Regarding your question about cell boundaries, we will revise the manuscript to specify that the boundaries we identified are those of each nucleus, rather than entire cells. This distinction will be made clear in the revised version.

### Reviewer #3 (Public review):

#### Weaknesses:

(1) *The work would have been strengthened by a more careful consideration of previous literature. Many papers directly relevant to this work were not cited. Such omissions do the authors a disservice because in some cases, they fail to consider relevant information that impacts the choice of reagents they have used or the conclusions they are drawing.*

*For example, when describing the antibody they use to label muscles (monoclonal 6G10), they do not cite the paper that generated this reagent (Ross et al PMID: PMC4307677), and instead, one of the papers they do cite (Cebria 2016) that does not mention this antibody. Ross et al reported that 6G10 does not label all body wall muscles equivalently, but rather "predominantly labels circular and diagonal fibers" (which is apparent in Figure S5A-D of the manuscript being reviewed here). For this reason, the authors of the paper showing different body wall muscle populations play different roles in body patterning (Scimone et al 2017, PMID: PMC6263039, also not cited in this paper) used this monoclonal in combination with a polyclonal antibody to label all body wall muscle types. Because their "pan-muscle" reagent does not label all muscle types equivalently, it calls into question their quantification of the different body wall muscle populations throughout the manuscript. It does not help matters that their initial description of the body wall muscle types fails to mention the layer of thin (inner) longitudinal muscles between the circular and diagonal muscles (Cebria 2016 and citations therein).*

*Ipsilateral and contralateral projections of the visual axons were beautifully shown by dye-tracing experiments (Okamoto et al 2005, PMID: 15930826). This paper should be cited when the authors report that they are corroborating the existence of ipsilateral and contralateral projections.*

Thank you for your feedback. We will incorporate these citations and clarifications into the revised manuscript. We acknowledge the limitations of this approach and recognize that it does not encompass all neuron types, particularly those involved in glutamatergic, glycinergic, and peptidergic signaling. We will also add the content about other neuron types in our revised version.

(2) *The proportional decrease of neurons with growth in *S. mediterranea* was shown by counting different cell types in macerated planarians (Baguna and Romero, 1981; <https://link.springer.com/article/10.1007/BF00026179>) and earlier histological observations cited there. These results have also been validated by single-cell sequencing (Emili et al, bioRxiv 2023, <https://www.biorxiv.org/content/10.1101/2023.11.01.565140v1>). Allometric growth of the planaria tail (the tail is proportionately longer in large vs small planaria) can explain this decrease in animal size. The authors never really discuss allometric growth in a way that would help readers unfamiliar with the system understand this.*



Thank you for your feedback. We will incorporate these citations and clarifications into the revised manuscript.

*(3) In some cases, the authors draw stronger conclusions than their results warrant. The authors claim that they are showing glial-muscle interactions, however, they do not provide any images of triple-stained samples labeling muscle, neurons, and glia, so it is impossible for the reader to judge whether the glial cells are interacting directly with body wall muscles or instead with the well-described submuscular nerve plexus. Their conclusion that neurons are unaffected by beta-cat or *inr-1* RNAi based on anti-phospho-Ser/Thr staining (Fig. 6E) is unconvincing. They claim that during regeneration "DV muscles initially regenerate into longitudinal fibers at the anterior tip" (line 373). They provide no evidence for such switching of muscle cell types, so it is unclear why they say this.*

We acknowledge that some of our conclusions were overclaimed given the current data, and we appreciate the opportunity to clarify and refine these claims in the revised manuscript. Regarding the statement that "DV muscles initially regenerate into longitudinal fibers at the anterior tip" (line 373), as addressed in our previous response, this phrasing was unclear. Our intent was not to imply that DV muscles switch into longitudinal fibers. Instead, we observed that muscle fibers reconnect at the wound site, with longitudinal fibers and other muscle types gradually restoring the structure. We will revise this section to better describe the dynamic changes observed during regeneration.

*(4) The authors show how their automated workflow compares to manual counts using PI-stained specimens (Figure S1T). I may have missed it, but I do not recall seeing a similar ground truth comparison for their muscle fiber counting workflow. I mention this because the segmented image of the posterior muscles in Figure 4I seems to be missing the vast majority of circular fibers visible to the naked eye in the original image.*

Thank you for raising this important point. We will include a ground truth comparison of our automated muscle fiber counting with manual counts in the supplementary figures. Regarding the observation of missing circular fibers in Figure 4I, we agree that the segmentation appears to have missed a significant number of circular fibers in this particular image. This may have been due to limitations in the current parameters of the segmentation algorithm, especially in distinguishing fibers in regions of varying intensity or overlap. We are revisiting the segmentation parameters to improve the accuracy of detecting circular fibers, and we will provide an updated version of Figure 4I in the revised manuscript.

*(5) It is unclear why the abstract says, "We found the rate of neuron cell proliferation tends to lag..." (line 25). The authors did not measure proliferation in this work and neurons do not proliferate in planaria.*

Thank you for bringing this to our attention. What we intended to convey was the increase in neuron number during homeostasis. We will revise the abstract to avoid this mistake in this context and instead describe it as the increase in neuron numbers due to progenitor cell differentiation during homeostasis.

*(6) It is unclear what readers are to make of the measurements of brain lobe angles. Why is this a useful measurement and what does it tell us?*

The measurement of brain lobe angles is intended to provide a quantitative assessment of the growth and morphological changes of the planarian brain during regeneration. Additionally,

the relevance of brain lobe angles has been explored in previous studies, such as Arnold et al., Nature, 2016, further supporting its use as a meaningful parameter.

*(7) The authors repeatedly say that this work lets them investigate planarians at the single-cell level, but they don't really make the case that they are seeing things that haven't already been described at the single-cell level using standard confocal microscopy.*

Thank you for your comment. We agree that single-cell level imaging has been previously achieved in planarians using conventional confocal microscopy. However, our goal was to extend the application of expansion microscopy by combining C-MAP with tiling light sheet microscopy (TLSM), which allows for faster and high-resolution 3D imaging of whole-mount planarians. This combination offers several key advantages over traditional confocal microscopy. For example, it enables high-throughput imaging across entire organisms with a level of detail and speed that is not easily achieved using confocal methods. This approach allows us to investigate the planarian nervous system at multiple developmental and regenerative stages in a more comprehensive manner, capturing large-scale structures while preserving fine cellular details. The ability to rapidly image whole planarians in 3D with this resolution provides a more efficient workflow for studying complex biological processes. We believe this distinction is significant and represents an advance over previous methods. We will clarify this point in the manuscript to better distinguish our approach from standard techniques.

<https://doi.org/10.7554/eLife.101103.1.sa0>